Turbulence and mixing in unsteady breaking surface waves

DAVID A. DRAZEN† AND W. KENDALL MELVILLE

Scripps Institution of Oceanography, University of California, San Diego, La Jolla,
CA 92093-0213, USA

Laboratory measurements of the post-breaking velocity field due to unsteady deep-water breaking are presented. Digital particle image velocimetry (DPIV) is used to measure the entire post-breaking turbulent cloud with high-resolution imagery permitting the measurement of scales from $O(1\,\text{m})$ down to $O(1\,\text{mm})$. Ensemble-averaged quantities including mean velocity, turbulent kinetic energy (TKE) density and Reynolds stress are presented and compare favourably with the results of Melville, Veron & White (*J. Fluid Mech.*, vol. 454, 2002, pp. 203–233; MVW). However, due to limited resolution, MVW's measurements were not spatially coherent across the turbulent cloud, and this restricted their ability to compute turbulent wavenumber spectra. Statistical spatial quantities including the integral length scale L_{11}, Taylor microscale λ_f and the Taylor microscale Reynolds number Re_λ are presented. Estimation of an eddy viscosity for the breaking event is also given based on analysis of the image data. Turbulent wavenumber spectra are computed and within 12 wave periods after breaking exhibit what have been termed 'spectral bumps' in the turbulence literature. These local maxima in the spectra are thought to be caused by an imbalance between the transport of energy from large scales and the dissipation at small scales. Estimates of the dissipation rate per unit mass are computed using both direct and indirect methods. Horizontally averaged terms in the TKE budget are also presented up to 27 wave periods after breaking and are discussed with regard to the dynamics of the post-breaking flow. Comparisons of the TKE density in the streamwise and cross-stream planes with the three-dimensional full TKE density are given in an appendix.

1. Introduction

Wave breaking at the ocean surface mixes surface waters, generates currents, limits the height of surface waves and dissipates surface-wave energy. Increased knowledge of the structure and evolution of the turbulent field in this regime is essential in order to further understand the role of breaking in air–sea interaction and in the formation of the marine boundary layer. The intermittent nature of breaking makes detailed field measurements with high spatial and temporal resolution very difficult. The laboratory provides us with a well-controlled environment in which high-precision, high-resolution measurements can be conducted in order to better understand the kinematics and dynamics of breaking and their relationship to breaking-generated turbulence. Progress in breaking-wave research has been reviewed several times in

---

† Present address: Naval Surface Warfare Center, Carderock Division, 9500 MacArthur Blvd, West Bethesda, MD 20817, USA. Email address for correspondence: david.drazen@navy.mil

recent years (Banner & Peregrine 1993; Melville 1996; Duncan 2001). However, we know very little about the turbulence generated by unsteady deep-water breaking waves, especially when compared to quasi-periodic breaking waves in shallow water.

In introducing the relevant literature we will concentrate on unsteady deep-water breaking. However, related literature on quasi-steady or quasi-periodic breaking in shallow water may be relevant for specific processes. This literature includes Duncan (1981, 1983), Lin & Rockwell (1995), and Chang & Liu (1998, 1999).

Bonmarin (1989) used cinematography of unsteady breaking waves to describe the various stages of breaking. A number of geometrical parameters were used to describe the asymmetry and steepness of the waves as they approached breaking. The shape of the plunging jet and the subsequent splash-up were also investigated, giving insight into the source of the post-breaking vorticity in relation to the plunging jet.

Rapp & Melville (1990; RM) measured turbulence generated by unsteady breaking waves in the laboratory. Simple flow visualization using dye permitted estimates of the extent of mixing by breaking as well as the rate of growth of the turbulent patch. They employed laser Doppler anemometry (LDA) on a regular grid in a number of realizations of the flow. While the grid spacing was coarse compared to modern digital particle image velocimetry (DPIV) standards, a coherent vortex structure was seen in the ensemble-averaged velocity field. Wave energy budgets showed that approximately 90 % of the energy from the breaking event was dissipated within four wave periods. The turbulent kinetic energy (TKE) was found to subsequently decay like t^{-1}, where t is the time after breaking. It was shown later by Lamarre & Melville (1991) that up to 50 % of the wave energy may be lost through work done in entraining air against buoyancy forces.

Perlin, He & Bernal (1996) used particle image velocimetry (PIV) and high-speed imagery techniques to measure the fine-scale structure of plunging breaking waves as the jet approaches the free surface. The maximum jet velocity was found to be approximately 30 % larger than the corresponding wave phase speed.

Veron & Melville (1999) used a coherent acoustic Doppler profiler to measure turbulence generated by unsteady breaking waves in both the laboratory and the field. Measurements of $u(x, t)$, the horizontal velocity component, were obtained at a depth of 10 cm below the mean water level in the direction of propagation. The turbulence was defined to be the residual velocity after the surface-wave-induced motions were filtered out. Evaluation of the wavenumber spectra showed the existence of an inertial sub-range with the dissipation rate ϵ decaying as t^{-n}, with n varying between 1 and 1.25. Gemmrich & Farmer (2004) also used a coherent acoustic Doppler profiler in the field and found the dissipation rate to decay as $t^{-4.3}$.

Melville *et al.* (2002; MVW) used DPIV to investigate the post-breaking velocity field under unsteady deep-water breaking waves in the laboratory. In order to describe the large-scale flow with sufficient resolution, a mosaic of images was used to reconstruct the ensemble-averaged velocity field. Analysis of this velocity field showed the existence of a large coherent vortex which propagated downstream under the influence of its image vortex above the surface. The TKE was found to decay with a t^{-1} dependence. These findings are consistent with the earlier LDA measurements of RM. The experiments of MVW were not specifically designed to measure the TKE budget, but with the exception of the pressure-work terms, an estimate of the balance of the terms was possible with an assumption of inertial-scale isotropy being used to compute the dissipation rate, ϵ. Comparison of horizontally integrated terms in the budget after the cessation of active breaking implied that a simple relationship

between production and dissipation in the turbulent cloud did not apply and that a likely balance between advection and turbulent transport existed. The dissipation rate evaluated from DPIV data was shown to agree with earlier estimates from Veron & Melville (1999).

The numerical simulation of breaking surface waves depends on results generated in the laboratory to help drive and validate models. Chen *et al.* (1999) conducted detailed two-dimensional simulations of plunging breaking waves past the point of impact. It was found that approximately 80 % of the wave energy was dissipated within three wave periods, and the temporal evolution of the energy was found to have a t^{-1} dependence, consistent with RM and MVW. The authors noted that their simulations were strictly two-dimensional, while the actual flows are inherently three-dimensional, perhaps accounting for the lower amount of energy lost ($\approx 80\%$) as compared to RM ($\approx 90\%$).

Watanabe, Saeki & Hosking (2005) have used large-eddy simulations (LES) to investigate vortex dynamics and kinematics in breaking shoaling waves. While the generation and evolution of vorticity in breaking flows is of great interest, such detailed analysis is currently beyond the scope of available measurements and is not pursued in this paper.

Sullivan, McWilliams & Melville (2004) developed a stochastic model of breaking waves which was evaluated through the use of direct numerical simulation (DNS). The Navier–Stokes equations were modified with an additional body force representing the local acceleration of the fluid due to breaking. The forcing was empirically defined and based on the laboratory results of RM and MVW. The simulations were run with breaking accounting for varying fractions of the total momentum flux across the surface, with the remaining fraction due to viscous stresses. It was found that a small fraction of active breaking caused significant turbulent mixing and vertical transport of horizontal momentum, with a strong dependence of the roughness length of the turbulent surface layer on the fraction of the momentum flux supported by breaking. Sullivan, McWilliams & Melville (2007) have recently extended this approach to include both breaking and Langmuir turbulence, demonstrating the significant interactions and similarities between the two phenomena.

An improved knowledge of the breaking at the ocean surface requires an understanding of the kinematics and dynamics of individual breakers as well as measurements of the statistics of breaking. While the statistics can only be measured in the field, detailed studies of the kinematics and dynamics can be carried out in the laboratory. The ability to make broadband measurements of breaking-wave-generated turbulence is of importance in understanding its role in upper ocean kinematics and dynamics. Advances in imaging and computer technology, even since the recent work of MVW, permit DPIV measurements with improved dynamic range in the wavenumber domain over larger ensembles of measurements.

We have revisited the experiments of RM and MVW using high-resolution digital imagery to capture a wide range of scales and a larger number of events in each ensemble to provide improved separation between the mean and turbulent fields while reducing errors in higher-order turbulent statistics. The resultant data set permits the measurement of ensemble-averaged quantities, wavenumber spectra and the structure of the turbulence and improved estimates of the TKE budget.

In §2 we describe the experimental set-up. We present ensemble-averaged flow variables in §3, measurements of turbulent length scales in §4, wavenumber spectra in §5 and terms in the TKE budget in §6. In §7 we discuss the significance of these results.

2. Experimental set-up

2.1. *Breaking-wave generation*

The experiments were carried out in the glass wave channel in the Hydraulics Laboratory at the Scripps Institution of Oceanography. The tank is 0.5 m wide, 1 m deep and 30 m long. See Drazen (2006) or Drazen, Melville & Lenain (2008; DML) for further details. The tank was filled to a working depth of 0.6 m with fresh water. A beach of 6° slope at the far end of the tank was coated with a thick fibrous mat to help dissipate surface wave energy.

Breaking waves were generated using the dispersive-focusing method first proposed by Longuet-Higgins (1974) and exploited by RM and others. A given wave packet has separate frequency components spread across a normalized bandwidth of $\Delta f/f_c$ centred at a frequency of f_c. The location and time of breaking according to linear theory are given by x_b and t_b, respectively.

Following Loewen & Melville (1991), we assigned a constant slope to each component of the wave packet rather than the constant amplitude formulation of RM.

The centre frequency of the wave packet was $f_c = 1.08$ Hz, the non-dimensional bandwidth was $\Delta f/f_c = 0.75$, and the non-dimensional distance to breaking was $x_b k_c = 40.5$. While the packet is long, the individual waves within the packet can be considered to be deep-water waves ($k_c H = 2.8$, where k_c is the wavenumber of the centre packet component and H the mean water depth). The non-dimensional time of breaking was $\sigma_c t_b = 118.9$, where $\sigma_c = 2\pi f_c$ is the radian centre frequency of the wave packet. The breaking wave generated was a plunging wave with an input slope of $S = 0.36$, which is the maximum slope at focussing according to linear theory. The need to generate a turbulent cloud that stayed within the measurement region for approximately 60 wave periods motivated the choice of parameters. A series of complementary experiments described by Drazen (2006) and Drazen, Melville & Lenain (2008) were designed to measure the dissipation rate of breaking surface waves over a larger range of parameter space. Measurement of quantities related to the bulk properties of the flow, including wave potential energy, wave energy fluxes and wave dissipation rates, along with more complete experimental details are given in those references.

2.2. *Digital particle image velocimetry*

The experiments described here were conducted within a 3.11 m long window starting 8.6 m from the wave paddle. We conducted two sets of experiments in the vertical longitudinal ($x−z$) plane, the first of which was designed to directly image the largest scales of the flow. A second set of experiments investigated the effects of increasing resolution on measurement of the turbulent fields, through the use of four overlapping windows. Measurements of the velocity field in the transverse ($y−z$) plane were conducted at four locations in order to quantify the cross-stream structure of the flow as well as provide measurements of the three components of velocity, (u, v, w), at the intersection of the longitudinal and transverse planes.

2.2.1. *Digital particle image velocimetry system*

The DPIV system utilized a 200 mJ Nd:YAG laser (New-Wave Gemini) to create a light sheet introduced from below the tank which was redirected to the vertical plane via a front-surface mirror. The light-sheet-generating optics (Dantec Dynamics 80 × 66, 80 × 64) created a 60° beam with a focussing distance of 0.7–3 m. The light sheet was reflected by a mirror to generate a light sheet in the longitudinal or transverse

planes (see Drazen 2006 for further details). Silver-coated glass (14 μm, 1.7 g cm^{-3}) or ceramic (100 μm, 1.01 g cm^{-3}) spheres (Potters Industries, AG-SL150-30-TRD, SH400S33) were used to seed the flow. The inside of the far wall of the test section (relative to the camera in the longitudinal plane) was painted with flat black paint to prevent reflections back to the camera.

Laser timing, triggering, image recording and image processing were performed through a commercially available DPIV software package, PixelFlow (VioSense Corporation). Data were recorded for 89 s, and there was a delay of approximately 10 min between experiments during which time the images were written to hard disk and the residual turbulence in the channel decayed.

The laser beam has a Gaussian intensity profile, and when spread across such a large region there are observable variations in the light-sheet intensity. In order to remove this non-uniform background intensity the images were first low-pass filtered using a method similar to the image pre-processing technique used by Willert (1997) without the subsequent binarization of the image.

Optical calibration of the system was performed using a Plexiglas sheet placed within the measurement plane. For the large-scale longitudinal measurements, two rows of 2 mm diameter holes were spaced 10 cm horizontally across the field of view. For the mosaic DPIV and DPIV in the transverse plane, a smaller grid with lines etched every 5 cm was used. The cameras were placed slightly below the water level and angled upwards in order to image the intersection of the light sheet with the free surface. The measured control points allowed for rectification of the images to account for any perspective distortion or refraction at the air–glass–water interface, through use of a projective or third-order polynomial transformation (Gonzalez & Woods 2002).

2.2.2. *The longitudinal plane (full-field)*

To directly capture the entire turbulent velocity field in the longitudinal plane a 3 Hz 4024 × 2560 charged-couple device (CCD) camera (VDS Vosskühler CCD-11000) with a 50 mm f1.4 lens was used, yielding a final resolution of 0.5 mm pixel^{-1}. The long axis of the CCD was aligned in the x-direction. A light sheet approximately 2 m long at the mean water level and 0.6 m in height was generated along the centreline of the tank. The seeding particles were 100 μm in diameter, and the thickness of the sheet varied from 3 mm at the bottom of the tank to 6 mm at the surface, which ensured that particles stayed within the sheet between a pair of images.

Two sets of runs were taken using a frame-straddling approach in which the time between laser pulses Δt was less than the reciprocal of the camera frame rate. The first run had 41 repeats with a time difference between image pairs of $\Delta t = 20$ ms, and a second had 32 repeats using a time difference of $\Delta t = 30$ ms. Concerns over the existence of peak-locking (Raffel, Willert & Kompenhans 1998) motivated the two separate sets. These two sets were combined to yield an ensemble of 73 repeats in the longitudinal plane, which enabled measurement of the relative error for a projected ensemble of approximately 40 repeats for the transverse plane and mosaic experiments. The normalized error in the magnitude of the velocity in the x-direction at the Nth repeat relative to the $N = 73$ ensemble is given by

$$\delta u_N = \sqrt{\sum_{kl} \frac{\left|u_{kl}^N - u_{kl}^{73}\right|^2}{\left|u_{kl}^{73}\right|^2}}, \qquad (2.1)$$

where the sum is over all of the $k \times l$ vectors in the matrix. The normalized error of second-order and third-order quantities at the Nth repeat relative to the $N = 73$ ensemble are given by

$$\delta Q_N = \sum_{kl} \frac{\left| Q_{kl}^N - Q_{kl}^{73} \right|}{\left| Q_{kl}^{73} \right|}, \tag{2.2}$$

where Q is either $1/2(\langle u^2 \rangle + \langle w^2 \rangle)$ or $\langle u^3 \rangle$. The normalized mean velocity magnitude converges as $N^{-0.61}$, the normalized TKE density as $N^{-0.55}$ and the normalized third-order correlation term as $N^{-0.50}$.

2.2.3. *The longitudinal plane (mosaic)*

The full-field DPIV measurements permitted direct measurement of a number of scales of the flow, with the focus on the largest scales. Due to the resolution of the camera we were therefore unable to resolve the smallest scales of the flow. We then extended the resolution of the measurements in the longitudinal plane using a technique similar to that used by MVW. A mosaic of measurements was taken with four overlapping images in the x-direction yielding an increase in resolution to 0.19 mm pixel^{-1}. The camera was mounted on a linear track parallel to the tank, with the long axis of the camera sensor orientated in the z-direction. In order to insure that these measurements were all made in the same plane the laser sheet illuminated the same region as the full-field measurements despite the smaller field of view.

The Δt was kept fixed at 30 ms, and 14 μm particles were used to seed the flow. Thirty-eight realizations of the flow were collected for each window, yielding normalized errors of 6.6 % for the velocity, 11 % for the TKE density and 65 % for the third-order correlations when referred to the ensemble average using all 73 realizations (see (2.1) and (2.2)).

Because the light sheet illuminated the entire full-field region, the overall illumination level within the fourth window was reduced. The camera gain was increased to attempt to compensate for this. Upon analysing the results it was found that due to a low signal to noise ratio in the images the measurements taken within this fourth window exhibited more noise than the previous windows for a given run. However, the turbulent cloud did not enter the fourth window for $(t - t_b)/T < 12.78$. We therefore restricted our analysis of the mosaic DPIV to the first three windows.

2.2.4. *The transverse plane*

A series of measurements in the transverse plane was conducted at four locations, $x = [8.98, 9.22, 9.42, 9.91]$ m, which correspond to $(x - x_b)/\lambda_c = [0.39, 0.57, 0.73, 1.09]$, where λ_c is the wavelength of the centre wave component. In the transverse plane a 1024×1024 camera (Uniq UP1830) enclosed in a watertight housing was placed in the water 1.27 m downstream of the light sheet and run at a frame rate of 24 Hz. The camera was angled up slightly to ensure that the surface was within the field of view using a 12.5 mm f1.8 lens for a resolution of 0.5 mm pixel^{-1}. The need to directly image the entire width of the tank and the square image sensor meant that the maximum depth imaged was approximately $z/\lambda_c = -0.34$. However, this is deeper than the depth to which particles are mixed down by breaking (see figure 1b). The seeding particles are the same as those used in the mosaic DPIV. The light-sheet thickness was 4 mm and $\Delta t = 30$ ms. The surface-wave-induced velocities can cause large out-of-plane motions, which was only an issue for the furthest downstream location (4) at $(t - t_b)/T = 3.42, 5.58$. A minimum of 37 realizations were collected
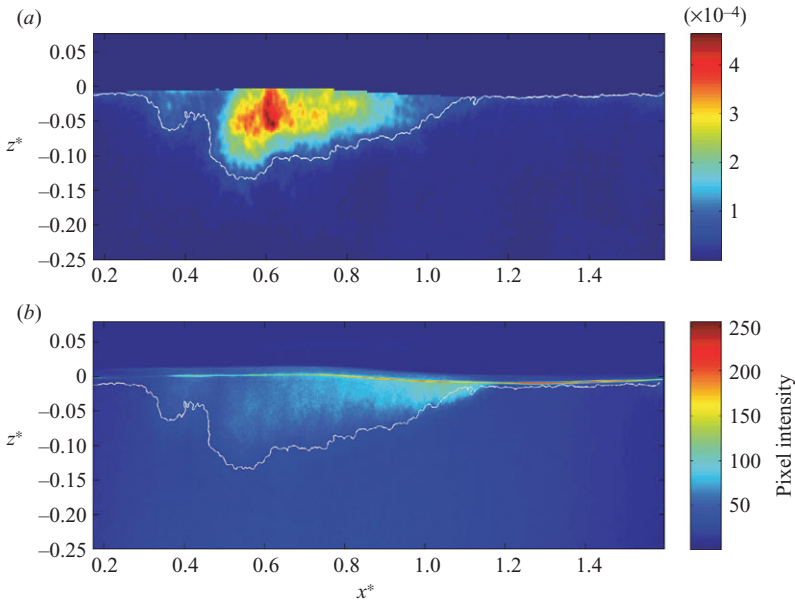
FIGURE 1. (*a*) Normalized TKE at 5.58 wave periods after breaking along with the $E_t = 8.22 \times 10^{-5}$ contour denoted in white (see (3.10)). (*b*) The ensemble-averaged DPIV images for 41 realizations at $t^* = 5.58$, showing the particles mixed down from the surface. The energy density contour from (*a*) is overlaid on the mean image in white. The vertical extent of particles mixed down from the surface by breaking correlates well with the turbulent cloud.

for each window with normalized errors of 6.8 % for the mean velocity field, 12 % for the TKE and 67 % for the turbulent energy flux.

2.2.5. *Digital particle image velocimetry processing*

Processing of the rectified image pairs was done using a multi-window method similar to DPIV-extended (DPIVE) described by MVW. The method starts with a window of 32×32 pixels (75 % overlap), and subsequent passes are made with smaller windows (16×16, 50 % overlap). Between each step the velocity field is corrected for outliers, and the final velocity field is smoothed with a 3×3 median filter before converting to laboratory coordinates. All sub-pixel interpolation is done using three-point Gaussian interpolation.

Determination of the surface profile for the cases considered is a simple matter when applied to an ensemble-averaged image. The interface between the laser sheet and the water surface has the brightest average return, and thus the free surface is the brightest point in each column (see figure 1*b*). The subsequent profile is then smoothed using a 32 pixel running mean filter. After processing has been performed, the values above the free surface are set to zero. Due to the configuration of the light sheet, non-illuminated regions in both the longitudinal and transverse planes exist. The vectors within these regions were also set to zero.

When dealing with a large field of view, difficulties arise in finding particles with an optimum size distribution and density. If the particle images are too small for the sub-pixel estimator, then peak-locking can result (Raffel *et al.* 1998) in which the particle displacement is biased towards an integer value. The amount of peak-locking is dependent on the sub-pixel estimator and the diameter of the individual particle

image. The cause of peak-locking is the inability of the chosen sub-pixel estimator to accurately resolve the peak of the cross-correlation.

Chang & Liu (2000) found bias errors which were as large as the turbulent intensities and thus called it 'psuedo-turbulence'. They attributed the cause of this psuedo-turbulence in their data to a bias error similar to this peak-locking effect. The resolution of our large-scale measurements in the longitudinal plane is lower than that of Chang & Liu (2000); however, we have larger seeding particles and a longer Δt which reduces this error.

As described in the experimental set-up, peak-locking in our measurements was a concern. Inspection of the velocity field showed that the peak-locking was only measurable outside the turbulent cloud and was an order of magnitude smaller than the TKE intensity within the cloud. Thus the bias error introduced by the peak-locking does not affect our measurements, and when presenting any horizontally or vertically averaged quantities, the data will be windowed to only include the spatial extent of the turbulent cloud. The horizontal locations of these limits can be seen in figure 5 as solid vertical white lines. The pattern that arises outside of the turbulent cloud as seen in figures 4–6 at $t^* = 3.42$ is not entirely due to peak-locking. The low-pass filtering performed on the images enhances a pattern generated by the reflection of the laser light from the free surface. It is thought that the change in reflected light from one image to the next in a pair causes this pattern to arise in the processed data. We have computed root mean square (r.m.s.) values of (u, w) at four discrete locations corresponding to peaks and valleys of the pattern at $t^* = 3.43$. The average r.m.s. values are $(4.1 \, \text{mm s}^{-1}, 3.3 \, \text{mm s}^{-1})$ at the peaks and $(3.1 \, \text{mm s}^{-1}, 2.6 \, \text{mm s}^{-1})$ at the valleys. The maximum uncertainty is therefore $(1 \, \text{mm s}^{-1}, 0.7 \, \text{mm s}^{-1})$ within this region. An average r.m.s. value within the cloud is approximately 20 times larger. While the uncertainty caused by this pattern is small, processing of the data is windowed in order to minimize any effect of noise on the results.

2.3. *Turbulent kinetic energy density*

The turbulence was computed using a Reynolds decomposition of the velocity field with mean quantities determined by an ensemble average, denoted by angle brackets. The instantaneous field is denoted by $\tilde{u}_i(x, t) = U_i(x, t) + u_i(x, t)$, with $U_i(x, t) \equiv \langle \tilde{u}_i(x, t) \rangle$ the ensemble-averaged velocity and $u_i(x, t)$ the turbulent velocity field. Unless otherwise stated, all means are computed using a ensemble average, and these two terms will be used interchangeably.

The evolution of the kinetic energy density of the turbulence is given by

$$\frac{\partial}{\partial t} \left(\frac{1}{2} \langle u_i u_i \rangle \right) + \langle u_j \rangle \frac{\partial}{\partial x_j} \left(\frac{1}{2} \langle u_i u_i \rangle \right)$$

$$= -\frac{\partial}{\partial x_j} \left(\frac{1}{\rho} \langle u_j p \rangle + \frac{1}{2} \langle u_i u_i u_j \rangle - 2\nu \langle u_i s_{ij} \rangle \right) - \langle u_i u_j \rangle S_{ij} - 2\nu \langle s_{ij} s_{ij} \rangle \quad (2.3)$$

(Tennekes & Lumley 1972). Here S_{ij} is the mean strain rate,

$$S_{ij} = \left(\frac{\partial U_i}{\partial x_j} + \frac{\partial U_j}{\partial x_i} \right), \quad (2.4)$$

and s_{ij} the fluctuating rate of strain,

$$s_{ij} = \frac{1}{2} \left(\frac{\partial u_i}{\partial x_j} + \frac{\partial u_i}{\partial x_j} \right). \quad (2.5)$$

The terms on the left-hand side of (2.3) represent the evolution and the advection of the TKE in the turbulent cloud. The first three terms on the right-hand side of (2.3) describe the transport of the turbulence by pressure work, turbulence and viscosity. The fourth term is the production and plays the complementary role of the same term in the evolution of the kinetic energy density of the mean flow. The final term on the right-hand side is the dissipation and accounts for the ultimate dissipation of energy into heat through the action of viscosity.

3. Ensemble-averaged flow quantities

Unless otherwise stated, all quantities will be normalized using the characteristic centre wavelength λ_c, period T_c or the phase speed C_c of the wave packet. The centre component refers to the quantity associated with the centre frequency of the wave packet, f_c. The origin will be defined as the time and location of breaking, and the normalized length and time scales are

$$x^* = (x - x_b)/\lambda_c, \tag{3.1}$$
$$z^* = z/\lambda_c, \tag{3.2}$$
$$t^* = (t - t_b)/T_c. \tag{3.3}$$

In the longitudinal plane, the origin in the vertical direction is at the quiescent mean water level.

3.1. *Mean velocity*

Figure 2 shows the mean velocity field in the longitudinal plane. Figure 3 shows the mean flow streamlines superimposed on the magnitude of the mean velocity field. Times shown are from 3.42 to 58.86 wave periods after breaking. At $t^* = 3.42$ the surface waves passing through the measurement region dominate the velocity field. By $t^* = 12.78$ there is still evidence of surface waves, but a clearly defined vortex has formed at $x^* \approx 0.6$. As noted by MVW this vortical region grows in time and slowly propagates downstream under the influence of its image vortex above the surface. We can also see residual surface waves in the tank at $t^* = 50.22$ and 58.86 with a frequency of $f \approx 1.8-2$ Hz. These are consistent with high-frequency free waves around the second harmonic generated by the breaking event propagating downstream through the measurement window (cf. RM).

The contours of the streamfunction Ψ show a well-defined coherent vortex at $t^* = 12.78$. Assuming the mean flow to be incompressible and two-dimensional the streamlines were computed using

$$\Psi = \left\langle \int (\tilde{u}\,dz - \tilde{w}\,dx) \right\rangle, \tag{3.4}$$

where $(\tilde{u}, \tilde{w})$ are the horizontal and vertical components of the velocity field. While surface waves are still in the tank, the vertical flow induced by the passing waves dominates the transverse flow field. Figures describing the transverse flow fields may be found in Drazen (2006). After the waves have propagated out of the region the mean flow exhibits transverse oscillations at $t^* = 43.02$ at all streamwise locations at which measurements were made in the cross-stream plane. These near-surface fluctuations are also seen at $t^* = 58.86$ and may be caused by the residual surface waves propagating within the tank. As the core of the vortex nears the fourth transverse location a downward flow is seen consistent with the clockwise rotation of the vortex in the $x-z$ plane. The magnitude of the velocity field and the corresponding
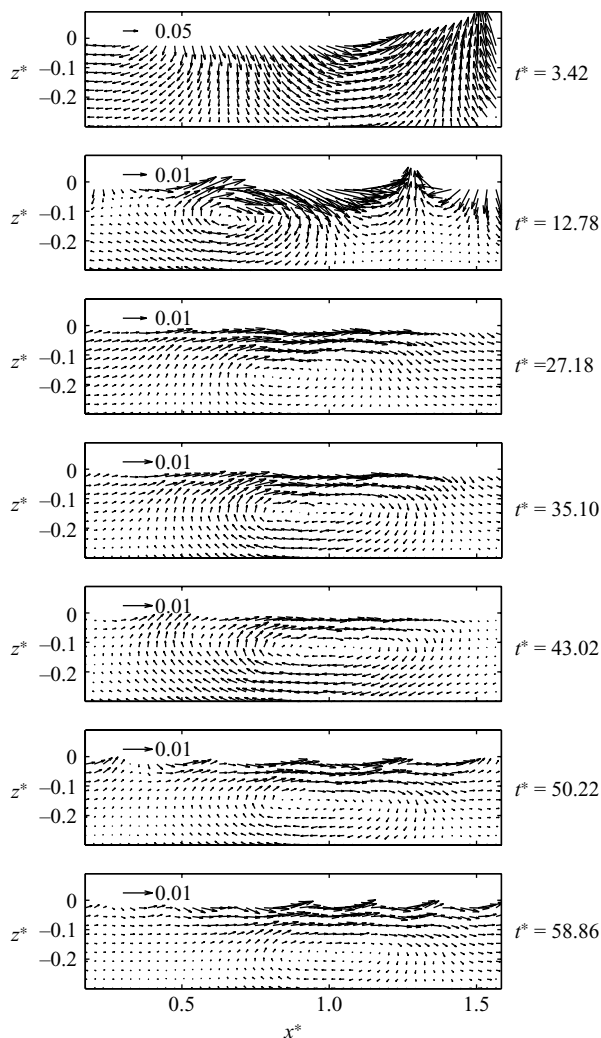
FIGURE 2. The normalized mean velocity field at $t^* = [3.42, 12.78, 27.18, 35.10, 43.02, 50.22, 58.86]$. The velocity fields are decimated by a factor of 10 in the horizontal direction and by a factor of 5 in the vertical direction for ease of interpretation. The velocity field induced by the surface waves is seen to be dominant up to approximately 12 wave periods after breaking.

streamlines do not exhibit any strong gradients in the y-direction, consistent with a flow that is two-dimensional in the mean.

3.2. Vorticity

The magnitude of the mean vorticity of the flow is shown in the left-hand column of figure 4. The vorticity is computed by calculating the circulation around a 3×3 grid divided by the area enclosed. Positive vorticity here corresponds to a counterclockwise rotation, and the large region of negative vorticity seen is consistent with the coherent structure seen in RM and MVW. A thin layer of positive vorticity is found at the surface and is thought to be an artefact of processing due to the proximity of the free surface.
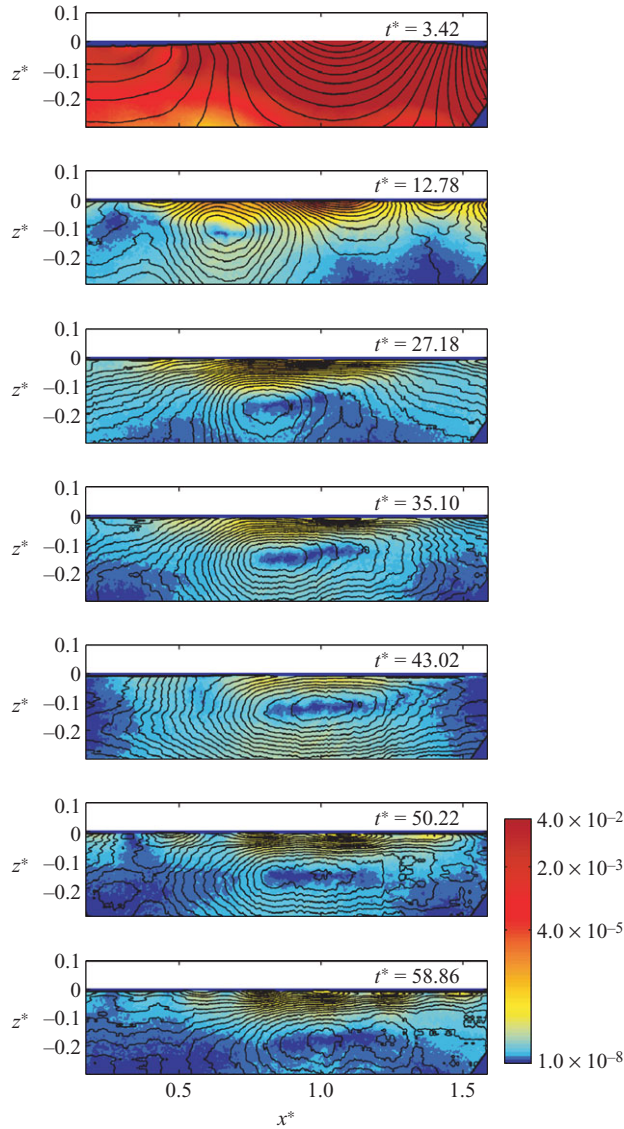
FIGURE 3. The normalized magnitude of the mean velocity field superimposed with the flow streamlines at the same times. The coherent vortex generated by the breaking process is clearly seen here after approximately 12 wave periods.

The mean square vorticity (twice the enstrophy) is given by

$$\mathcal{W} = \langle (\Omega + \omega)^2 \rangle \tag{3.5}$$

$$= \Omega^2 + \langle \omega^2 \rangle \tag{3.6}$$

$$= \mathcal{W}_m + \mathcal{W}_t, \tag{3.7}$$

where ω is the magnitude of the out-of-plane component of vorticity and $\Omega = \langle \omega \rangle$; $\mathcal{W}_m$ is the squared mean vorticity; and $\mathcal{W}_t$ the mean squared turbulent vorticity.

We show the mean squared turbulent vorticity in the longitudinal plane in the right-hand column of figure 4. If the flow was fully resolved we could consider the
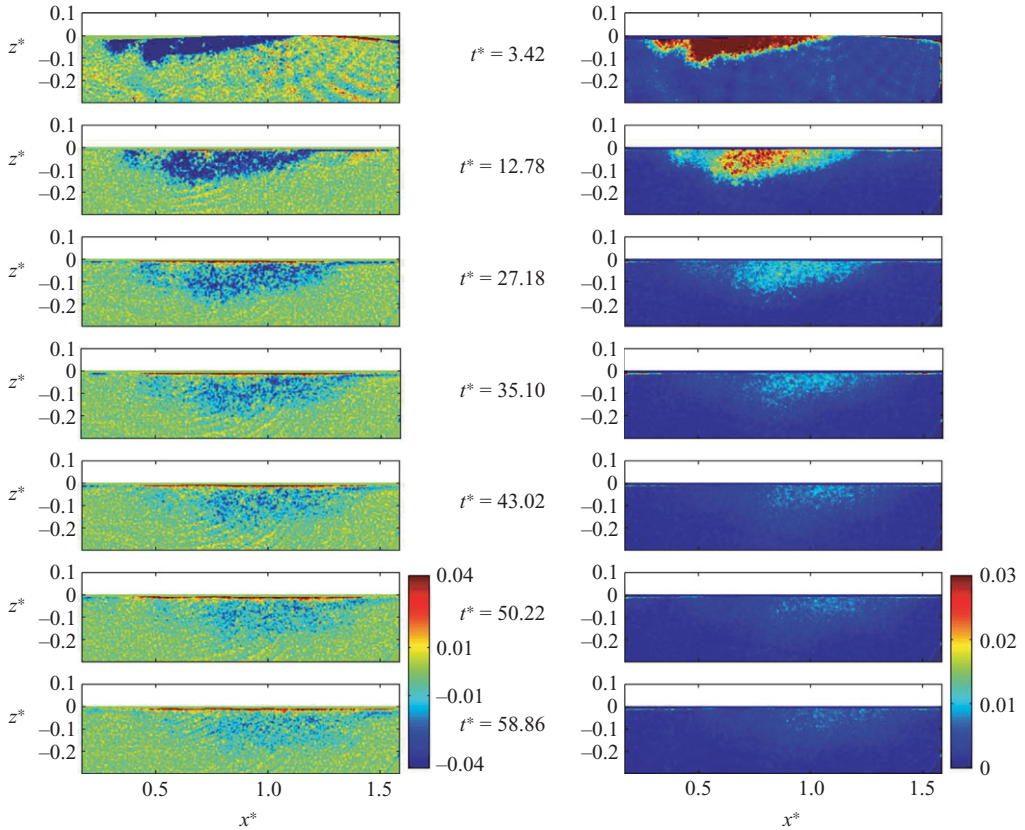
FIGURE 4. The left-hand column is the normalized magnitude of the vorticity of the mean flow, and the right-hand column is the normalized mean squared turbulent vorticity, $\mathcal{W}_t$, or twice the enstrophy. The vorticity is mainly negative (corresponding to clockwise rotation) and deepens slowly as the turbulent cloud propagates downstream. The squared turbulent vorticity is concentrated in regions of high TKE and rapidly decreases with time. The pattern in the background which dominates at $t^* = 3.42$, and less so for later t^*, is thought to be caused by a pattern generated when the light sheet reflects off the free surface (see § 2.2.5 for further discussion).

mean squared turbulent vorticity to be a proxy for the dissipation. At the current resolution we cannot resolve the dissipative scales comparable to the Kolmogorov length scale η_k (not to be confused with the surface elevation η). We can see however that the region over which it is significant is well correlated with the turbulent cloud and is advected downstream with the coherent structure generated by breaking.

The streamwise component of the mean squared turbulent vorticity measured in the transverse plane is approximately homogeneous across the channel and reinforces the notion that the flow after $t^* = 3.42$ is two-dimensional in the mean.

3.3. *Kinetic energy*

The mean kinetic energy density of the flow is given by

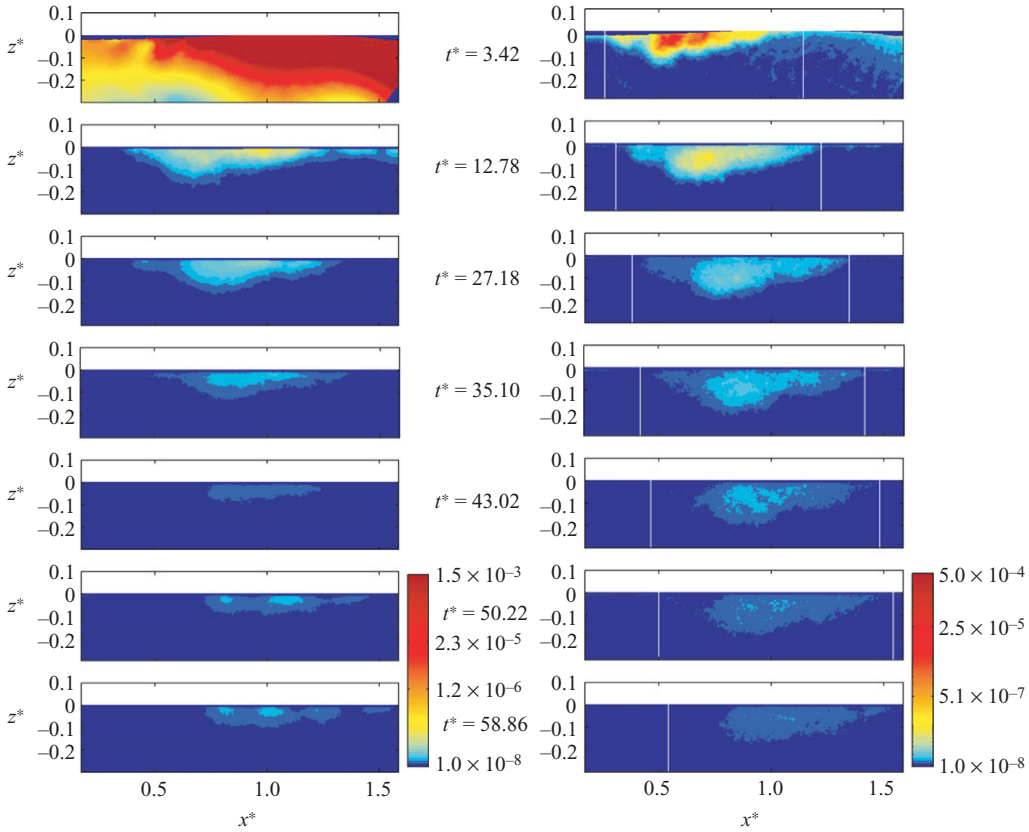$$E = \frac{1}{2} \left\langle (U_i + u_i)^2 \right\rangle \tag{3.8}$$

FIGURE 5. The left-hand column is the normalized kinetic energy density of the mean flow. The right-hand column is the normalized TKE density. The turbulent cloud can be seen to slowly deepen and move downstream. The vertical white lines denote the horizontal limits used when computing various turbulent statistics. The width of these limits grows in time and moves with the cloud.

$$= \frac{1}{2}U_i^2 + \frac{1}{2}\left\langle u_i^2 \right\rangle \tag{3.9}$$

$$= E_m + E_t, \tag{3.10}$$

where E_m and E_t are the respective kinetic energy densities of the mean flow and the turbulence.

The kinetic energy density of the mean flow in the longitudinal plane $1/2\left(U^2 + W^2\right)$ is presented in the left-hand column of figure 5 and kinetic energy density of the corresponding turbulence, $1/2(\langle u^2 \rangle + \langle w^2 \rangle)$, in the right-hand column. The initial levels of kinetic energy of the mean flow are quite large due to the presence of surface waves, and a logarithmic color scale is employed in order to encompass the entire dynamic range of the kinetic energy density. The cloud of kinetic energy density for both the mean and turbulent flows is seen to propagate downstream at a rate consistent with the large coherent vortex generated by breaking.

The cloud of TKE reaches a depth of $z^* \approx -0.12$ at five wave periods after breaking with a horizontal extent of approximately $0.83\lambda_c$. The initial levels of TKE are seen to decrease quite rapidly with time. The vertical white lines in figure 5 denote the extent of the limits taken when windowing the data as described in §2.2.5.

Figure 1 shows a comparison between the TKE density at $t^* = 5.58$ and the corresponding ensemble-averaged image of the seeded flow. The outline of the turbulent cloud is delineated by the $E_t = 8.22 \times 10^{-5}$ contour, shown in white. This outline is overlaid on the image of the particles mixed down by the breaking event in figure 1(b). Two distinct regions are seen just upstream and downstream of $x^* = 0.4$. The shallower upstream bump corresponds to the initial plunge point of the breaking wave, while the downstream region is due to the subsequent splash up (cf. Bonmarin 1989; Rapp & Melville 1990; Chen *et al.* 1999).

Within a few wave periods the kinetic energy of the mean flow in the transverse plane is approximately uniform across the tank. There is some horizontal variability in the transverse TKE field, significantly less however than the inhomogeneity seen in the longitudinal plane. It was thought that cross-stream structures might be generated by a transverse instability similar to that seen by Loewen (1991), Lamarre (1993) and Perlin *et al.* (1996). It is possible that cross-stream structures are generated by breaking which then rapidly dissipate and thus would not be seen for the times investigated here.

3.4. *Reynolds stress*

The Reynolds stresses transfer momentum from the surface wave field into the bulk of the fluid. The Reynolds stress component in the longitudinal plane $\langle uw \rangle$ is shown in figure 6 and is overwhelmingly negative, consistent with the findings of RM and MVW. It is this mechanism through which currents are generated by breaking due to the vertical flux of horizontal momentum lost from the waves.

In the absence of coherent transverse flow structures, $\langle vw \rangle$ in the transverse plane is expected to be zero. Figure 7 shows the integrated Reynolds stress is essentially zero in the four transverse planes with no net transport of momentum. The exception to this is for small t^* during which there may be transverse waves excited by breaking that would break the symmetry of the flow.

MVW additionally used measurements of the Reynolds stress to infer a value of the breaking parameter b as defined by Phillips (1985)(see also Duncan 1981, 1983). For the sake of brevity we will not outline the process used by MVW to arrive at b. Rather we simply will provide the reader with an overview and the results and refer those interested in the details to the reference.

Phillips (1985) proposed a statistical description of breaking based on the distribution by velocity of breaking fronts per unit area of ocean surface. The average rate of energy loss per unit area of surface for breaking waves with velocities in the range $(c, c + dc)$ is then

$$\epsilon(c)\,dc = b\rho g^{-1} c^5 \Lambda(c)\,dc, \qquad (3.11)$$

where $\Lambda(c)\,dc$ is the average length of breaking fronts per unit surface area, g gravity, c the speed of the advancing front and b the dimensionless breaking parameter. DML showed b to be dependent on the slope of the waves at breaking. MVW used measurements of the Reynolds stress to estimate the breaking parameter, b.

Using Phillips's (1985) distribution Λ_c the area swept out by breaking per unit area is given by $c\tau_b\Lambda(c)\,dc$, where τ_b is the duration of active breaking during which momentum is transferred from the surface waves to the fluid. MVW approximated the duration of breaking as a fraction of the wave period using data from RM.

Since the wave energy and momentum densities are related by $M = C_c^{-1}E$, use of (3.11) yields an estimate of b from the distribution of momentum flux as described
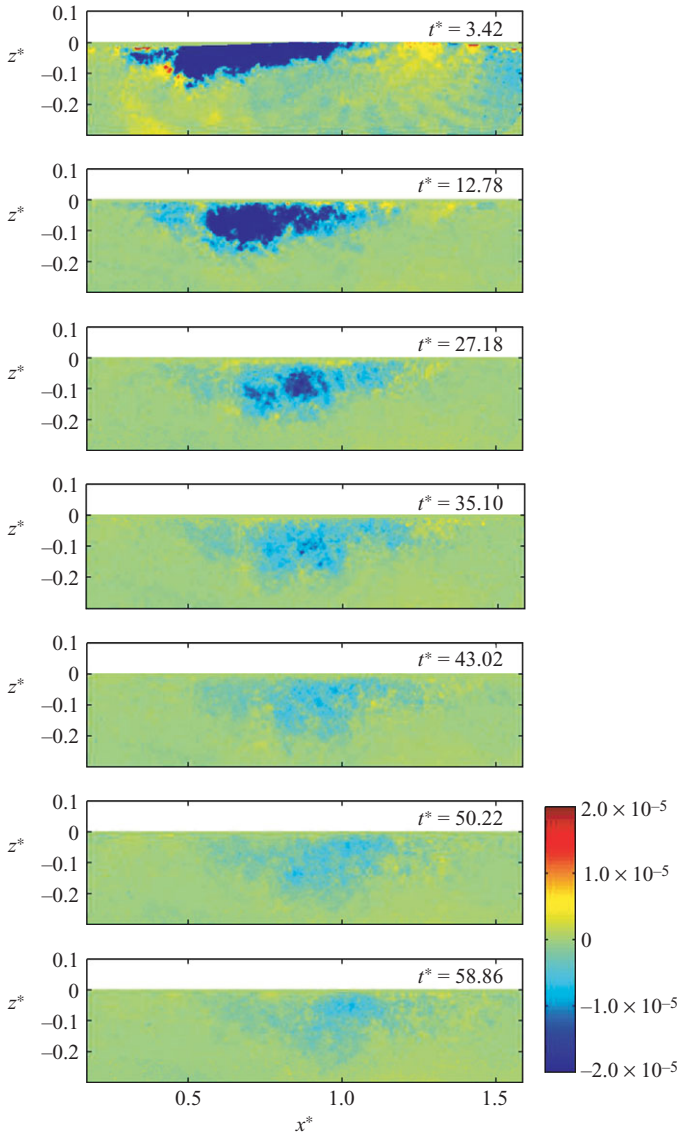
FIGURE 6. The normalized Reynolds stress in the longitudinal plane, $\langle uw \rangle$. The stress is predominately negative and corresponds to the vertical downward transport of positive horizontal momentum.

by MVW,

$$b = \mathscr{J} \frac{2\pi}{(0.67)^3} \frac{\iint uw \, \mathrm{d}x^* \mathrm{d}z^*}{C_c^2}, \tag{3.12}$$

where $\mathscr{J}$ is a numerical factor; C_c is the phase-speed of the centre wave component; and 0.67 arises from the ratio of the rate of advance of the breaking front and the centre phase speed of the wave packet.

An estimate of $\iint uw \, \mathrm{d}x^* \mathrm{d}z^*$ is computed from a time series at fixed z^* corresponding to the depth of the maximum Reynolds stress for $t^* = 3.42$ ($z^* = -0.03$). The temporal
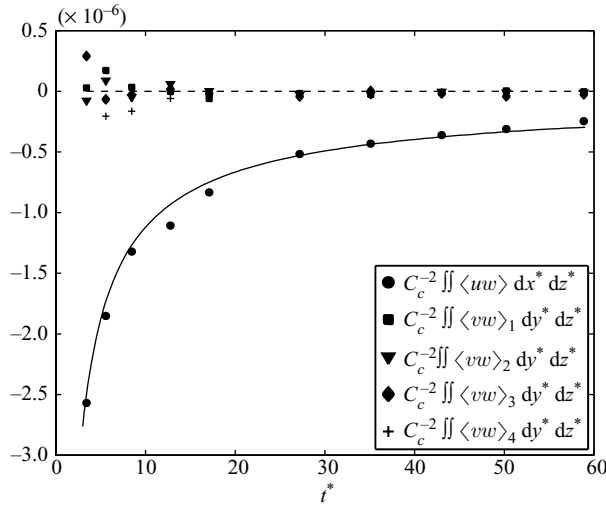
FIGURE 7. The integrated normalized Reynolds stress in both the longitudinal and transverse planes. The negative values of $\iint \langle uw \rangle \, dx \, dz$ correspond to a net downward transport of positive horizontal momentum. The net transport in each transverse plane is essentially zero except at small times (see §3.4). The subscripts refer to the location of the cross-stream measurement. The solid line is a $t^{-3/4}$ fit to the integrated Reynolds stress in the longitudinal plane.

spacing of the data presented is irregular, so we will fit a line to the integrated Reynolds stress and use this to compute the time average with an even spacing (as for figure 7). We find $b = 0.015$ which agrees within a factor of 1.5 with the measurement of $b = 0.022$ by DML for the wave packet considered. The prediction of b based on the inertial estimate of dissipation derived by DML is

$$b = \chi \pi 2^{-1/2} (hk_c)^{5/2}, \qquad (3.13)$$

where χ is a constant $O(1)$ and hk_c is the slope based on the height of the breaking wave (see DML for definition). For plunging breaking waves, χ was found to be 0.45, and hk_c for the wave packet considered in these DPIV measurements was 0.21. The value of b predicted by the model using (3.13) is then 0.021, as compared to $b = 0.015$ from (3.12).

3.5. *Time-dependence of turbulent kinetic energy and E_m*

Figure 8(*a*) presents integrated quantities of the total kinetic energy $\breve{E} = \breve{E}_t + \breve{E}_m$, TKE $\breve{E}_t$ and the kinetic energy of the mean flow $\breve{E}_m$, in the longitudinal plane in which the breve denotes an area integral. The area over which the integration was conducted was windowed horizontally over the limits shown in figure 5 and restricted to $z^* > -0.23$. The kinetic energy is initially large due to the surface waves which propagated through the measurement region. When $t^* \approx 12$, $\breve{E}$ and $\breve{E}_m$ begin to show a t^{-1} dependence, which is consistent with the findings of Rapp & Melville (1990), Chen *et al.* (1999) and Melville *et al.* (2002). The decay of $\breve{E}_t$ is slightly less rapid with an approximate $t^{-0.75}$ dependence. Prior to $t^* \approx 12$, there are still surface waves within the measurement region. We attribute the slower decay rate of TKE to their presence at the earlier times.

Figure 8(*b*) shows the integrated values of the TKE for both the full-field and higher resolution mosaic DPIV, denoted by $\breve{E}_{tF}$ and $\breve{E}_{tH}$ respectively. The intent of the
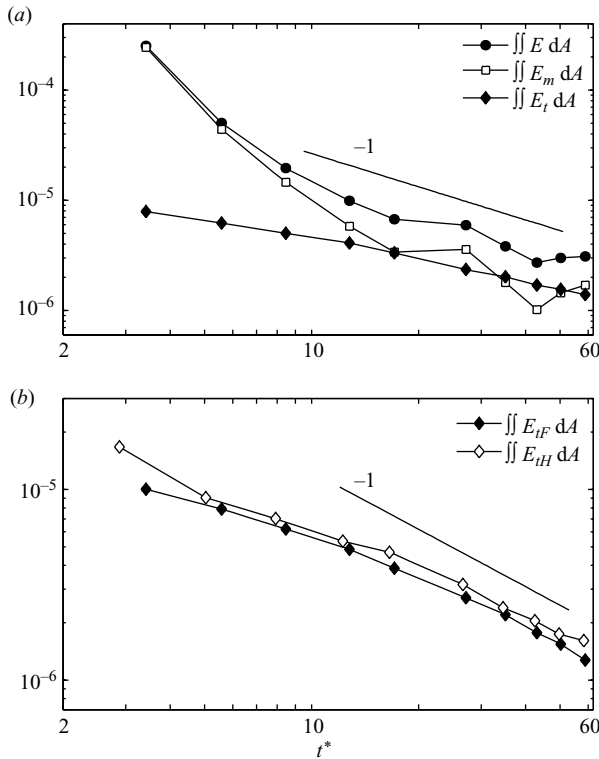
FIGURE 8. (a) $\check{E} = \check{E}_m + \check{E}_t$, $\check{E}_m$ and $\check{E}_t$ for the full-field DPIV measurements. The breve denotes an area integral. (b) Comparison between TKE of the full-field ($\check{E}_{tF}$) and high-resolution mosaic DPIV ($\check{E}_{tH}$).

full-field DPIV was to capture as large a range of scales as possible while resolving the largest scales of the flow. As a result of this, we were unable to measure the smallest scales; thus we employed a mosaic approach in order to resolve smaller length scales than we could with the full-field measurements. In order to compare these two results in the longitudinal plane, the full-field measurement is broken up into three windows corresponding to the same field of view as the mosaic DPIV. The integrated energy is calculated in each window, and these three estimates are then summed. Due to the slight overlap between windows in the mosaic DPIV the magnitude of the integrated TKE will be slightly higher in figure 8(b) than in figure 8(a), but the time dependence will not change. The full-field measurements extend to within 6 mm of the surface, while the mosaic DPIV is within 2.4 mm. The integrated TKE density curves have an approximate t^{-n} dependence for $t^* > 12.78$, where $0.75 < n < 1$, while for $t^* < 12.78$ the decay is slower and approximately $t^{-1/2}$.

3.5.1. *Estimation of ν_T*

The extent of the mixing caused by breaking can be better visualized by removing the displacement of the surface by the waves. We step through each ensemble-averaged image, column by column, and use the surface elevation to adjust each column up or down relative to the ensemble-averaged water level to generate an image in which the free surface is horizontal. These adjusted images are shown in figure 9 for $t^* = 0.54-2.70$. The mixed region consists of bubbles entrained by the breaking process and particles which have been mixed down from the surface. The boundary
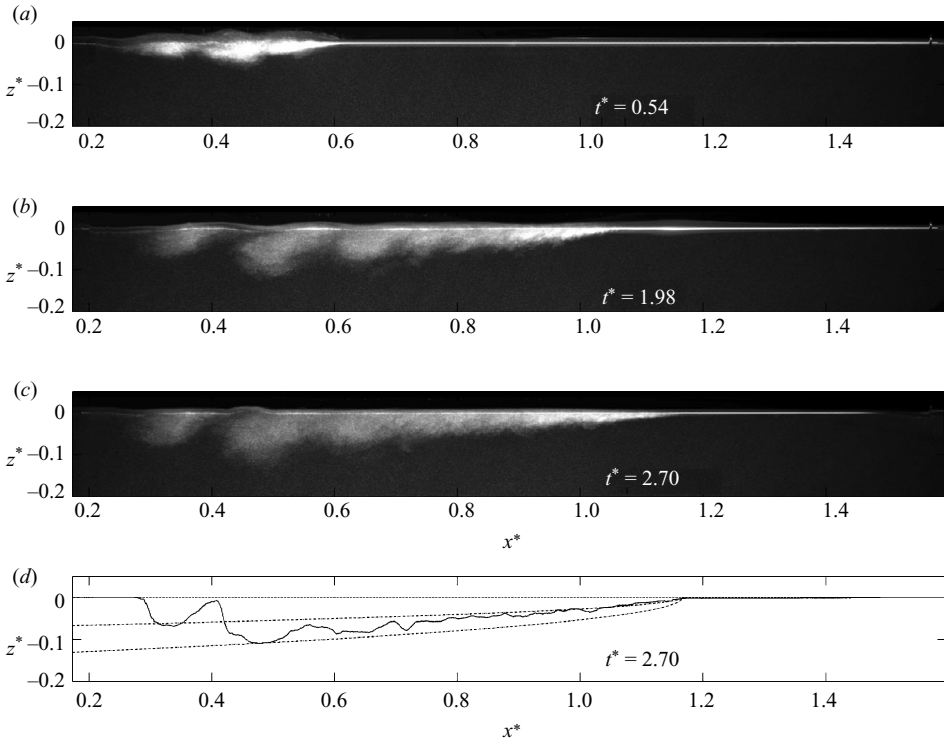
FIGURE 9. The raw ensemble-averaged image data (32 realizations) for $t^* = [0.54, 1.98, 2.70]$ (*a–c* respectively). The region mixed by breaking consists of air entrained by breaking along with tracer particles mixed down from the surface. Each image has been shifted vertically column by column to give the vertical position relative to the free surface. (*d*) The outline of the mixed region for $t^* = 2.70$ (*c*) superimposed with the boundary-layer thickness $\delta(x, t^* = 2.70)$ (solid line). Note that the large-scale structures survive the ensemble averaging. The dash-dotted lines denote the boundary-layer thickness corresponding to the range of ν_T for the given mixed region.

of the mixed layer shows an approximately $x^{1/2}$ dependence. We can estimate an eddy viscosity ν_T, using

$$\nu_T(x, t) = \frac{\delta^2(x, t) C_{bf}}{x}, \tag{3.14}$$

where δ is the thickness of the mixed layer; C_{bf} is the speed of the advancing breaking front; and x is the distance from the front.

The length of the mixed region versus t^* initially expands quite rapidly, $C_{bf} = 0.67 C_c$, where C_c is the centre phase speed of the packet. After $t^* \approx 3$ the length of the mixed region expands more slowly, $C_{bf} = 0.007 C_c$ (see Drazen 2006, figure IV.32). These results agree with the findings of RM, who found the initial speed to be $C_{bf} = 0.7 - 0.8 C_c$, which decreased to $C_{bf} = 0.005 - 0.01 C_c$ after three wave periods. The area of the mixed region obtained from the raw image files in figure 9 is seen to grow as $t^{1/2}$ matching the time dependence found by RM (see also Drazen 2006, figure IV.33).

The eddy viscosity is found by fitting the boundary-layer thickness to (3.14). The thickness of the boundary layer is seen to oscillate between the coherent structures or eddies in the ensemble-averaged flow, so a minimum and a maximum value of ν_T is found corresponding to the range of $\delta(x)$. Figure 9(*d*) shows the extracted boundary
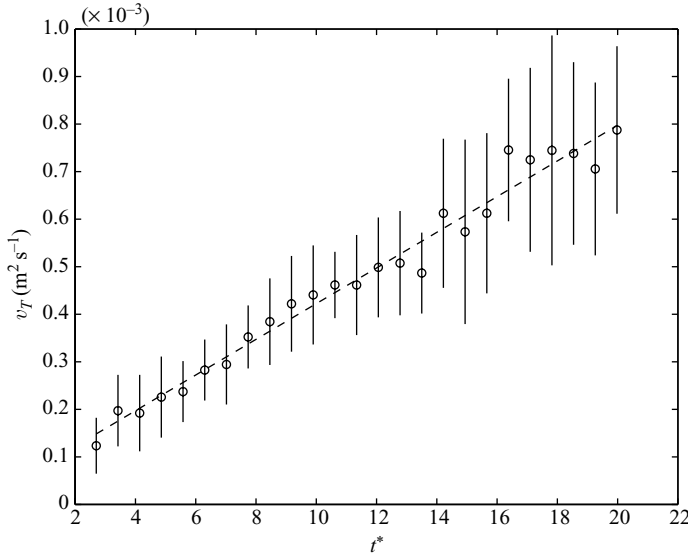
FIGURE 10. The non-normalized measured eddy viscosity, v_T, as a function of normalized time after breaking for $t^* \geqslant 2.70$. The vertical bars represent the maximum and minimum values of $v_T(t)$ (see figure 9d), and the dashed line is a least squares fit of the data to a straight line.

layer for $t^* = 2.70$ along with the boundary layers associated with the maximum and minimum values of v_T. The range of $v_T(t)$ is 1.2×10^{-4} to 7.9×10^{-4} m² s⁻¹ (figure 10). The eddy viscosity is seen to increase linearly in time with a slope of 0.4×10^{-4} m² s⁻² for $t^* > 2.70$ (figure 10).

4. Turbulent length scales

To aid in interpretation of the turbulence, it is useful to consider some representative length scales of the turbulent flow. For a given t^* and z^*, the longitudinal integral length scale L_{11} is defined as

$$L_{11} = \int_0^\infty \frac{\langle u(x+r)u(x) \rangle}{\langle u^2(x) \rangle} \, \mathrm{d}r, \tag{4.1}$$

with $u(x)$ being the longitudinal component of the turbulent velocity field at a specific depth and time. The integral length scale is a measure of the decorrelation length scale of the turbulence and is a characteristic length scale of the energetic eddies within the flow. The length scale L_{11} grows in time as seen in figure 11(a) and is evaluated at each time for both a fixed point within the flow, $(x^*, z^*) = (0.58, -0.034)$, and a location moving at the vertical speed of the coherent vortex, $-6.9 \times 10^{-4} C_c$. At a fixed location, separation of decay caused by the propagation of the cloud from that due to the loss of energy from the velocity field would be difficult. The average horizontal speed of the cloud is $7 \times 10^{-3} C_c$.

Another length scale derived from the velocity correlation is the Taylor microscale λ_f. By expanding the velocity correlation at the origin, λ_f can be seen to be the x-intercept of the parabola which osculates with the velocity correlation at the origin,

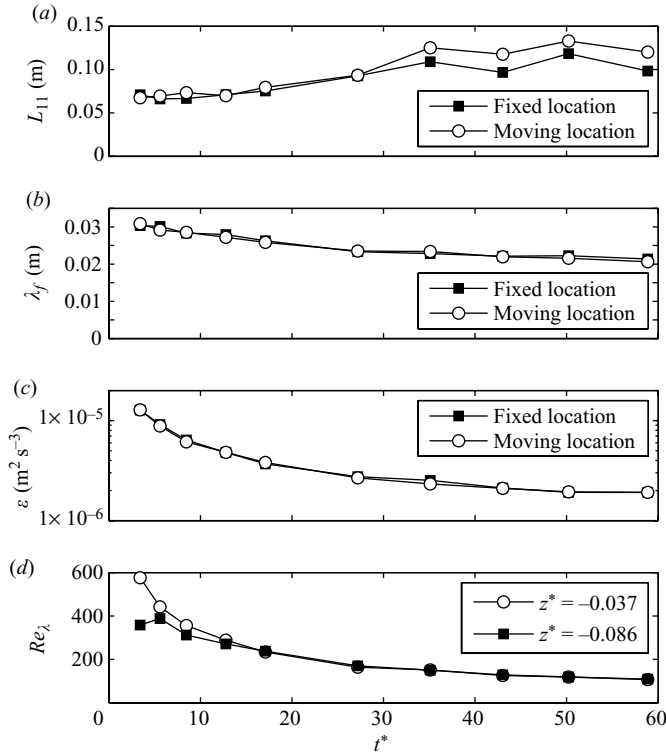$$\lambda_f = \left[-\frac{1}{2} f''(0) \right]^{-1/2}. \tag{4.2}$$

FIGURE 11. (a) L_{11}, (b) λ_f, (c) $\epsilon = 30 \nu u'^2/\lambda_f^2$ and (d) $Re_\lambda = (u'\lambda_f)/\nu$ as functions of non-dimensional time after breaking. For $(a-c)$ the open symbols correspond to a fixed point in the flow $(x^*, z^*) = (0.58, -0.034)$, while the measurement depth of the solid symbols followed the deepening of the TKE cloud. In (d) the open and filled symbols are for Re_λ at $z^* = [-0.083, -0.034]$ respectively.

In homogeneous, isotropic turbulence (4.2) reduces to

$$\lambda_f^2 = \frac{2u'^2}{\left\langle \left(\frac{\partial u}{\partial x}\right)^2 \right\rangle}, \qquad (4.3)$$

where u' is the r.m.s. value of the fluid velocity in the x-direction. For the flow considered here (4.3) was used to define λ_f in figure 11(b). The values of λ_f are seen to decrease with time and are approximately $L_{11}/5$. The dissipation rate in an isotropic, homogeneous flow is given by

$$\epsilon = 15\nu \left\langle \left(\frac{\partial u}{\partial x}\right)^2 \right\rangle \qquad (4.4)$$

$$= 30\nu \frac{u'^2}{\lambda_f^2} \qquad (4.5)$$

after substitution of (4.3) and is shown in figure 11(c). The flow here is however neither isotropic nor homogeneous, so these measures are only approximations. Veron & Melville (1999) and Melville et al. (2002) found dissipation rates of the same magnitude using coherent acoustic Doppler sonar and PIV, respectively. Approximately 17 wave

periods after breaking the estimate given by (4.5) was a factor of two larger than that reported by Veron & Melville (1999).

Note that the dissipation rate presented in figure 11(*c*) represents the dissipation rate for a homogeneous, isotropic flow with the same r.m.s. turbulence levels and Taylor microscale as this flow and should not be confused with the actual dissipation of the flow under consideration here. Despite the fact that our flow is not isotropic or homogeneous, comparison of our results with flows that have similar turbulence scales can be useful for order-of-magnitude estimates.

A Reynolds number based on the Taylor microscale is given by

$$Re_\lambda = \frac{u' \lambda_f}{\nu}. \tag{4.6}$$

Values of Re_λ for two depths are shown in figure 11(*d*) as functions of time. The value of Re_λ is initially large and asymptotically approaches 100 with t^* for for both depths. For large values of Re_λ in statistically stationary flows the separation between the energy-containing scales and the dissipative scales grows, a consequence of which is an enlarged inertial sub-range in which viscous effects are negligible (Pope 2000, figure 6.20). However, we do not have a statistically stationary flow and a relatively simple characterization of the conditions under which an inertial sub-range exists may not be possible.

5. Wavenumber spectra

The instantaneous large-scale measurements of the flow are well suited for computation of spectra over a large range of wavenumbers. The ensemble-averaged one-sided wavenumber spectra are calculated using

$$E_{ii}(k_j, t) = \frac{2}{XM} \sum_{m=1}^{M} |\hat{u}_i(k_j, t)|^2, \tag{5.1}$$

where X is the spatial length of the signal; k is the wavenumber; M is the number of realizations over which the spectrum is averaged; and $\hat{u}_i(k_j, t)$ is the fast Fourier transform (FFT) of $u_i(x_j, t)$. Prior to computing (5.1) all datasets in the x_i-direction are detrended and windowed using a Tukey window with a taper ratio of 0.2. Due to the inhomogeneity of the flow the limits of the window in the x_1-direction are set using the vertical lines seen in figure 5, so only the energetic portion of the flow is considered. The spectra in the z^*-direction extend from the free surface to $z^* = -0.23$.

5.1. *Measurements of E_{11} and E_{33}*

Spectra of E_{11} and E_{33} in the k_1-direction are shown in figure 12(*a*–*f*) for $z^* = -0.06$. The normalized times after breaking are the same as the first six times shown in the velocity and TKE fields, $t^* = 3.42$–50.22. We can see that for all t^* shown, the flow at low wavenumbers is anisotropic. The strain rate of the large eddies is comparable to that of the mean flow, and since the mean flow is anisotropic ($U > V, W$), the large eddies are anisotropic. For figure 12(*a, b*), there is some indication of isotropy for wavenumbers between 60 rad m^{-1} < k_1 < 200 rad m^{-1}, as the two spectra are nearly equal in magnitude. Within this wavenumber range, $E_{11}(k_1) = 0.78 E_{33}(k_1)$ for figure 12(*a*) and $E_{11}(k_1) = 0.87 E_{33}(k_1)$ for figure 12(*b*). For an isotropic flow, $E_{11}(k_1) = 3/4 E_{33}(k_1)$ (Pope 2000); however we do not think that these results are strong evidence for isotropy in this flow.
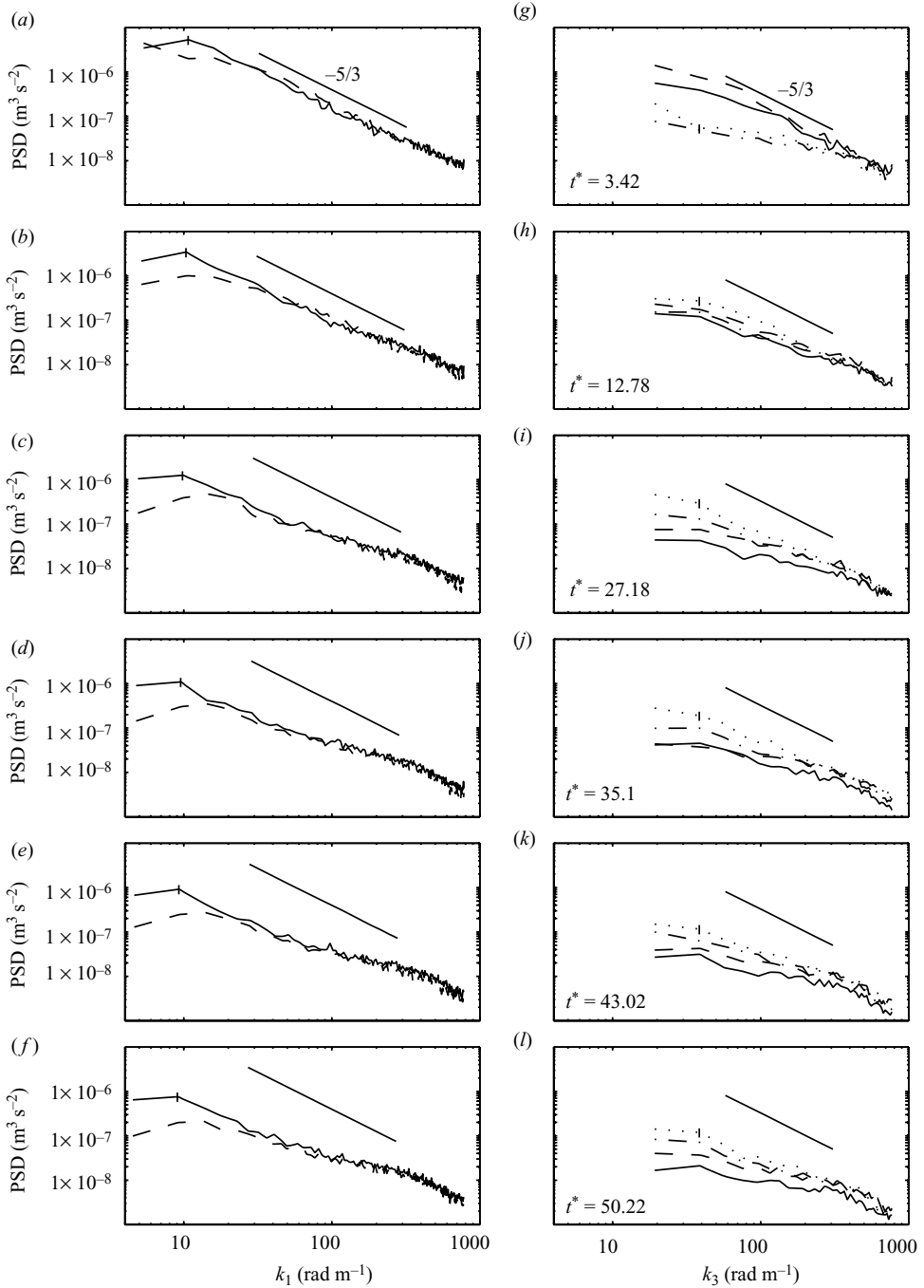
FIGURE 12. Comparison between one-dimensional wavenumber spectra in the (*a–f*) k_1- and (*g–l*) k_3-direction. The 95 % confidence levels are shown for each spectra at $k_1 = 10$ rad m^{-1} or $k_3 = 40$ rad m^{-1}. For each row the normalized time after breaking is constant and is denoted in (*g–l*). (*a–f*) $E_{11}(k_1)$ (——) and $E_{33}(k_1)$ (– –) at $z^* = -0.06$. (*g–l*) $E_{11}(k_3)$ (– –) and $E_{33}(k_3)$ (——) at $x^* = 0.54$ and $E_{11}(k_3)$ (· · ·) and $E_{33}(k_3)$ (– · –) at $x^* = 0.84$. The solid line in each figure has a slope of $-5/3$ and is kept at a fixed location.

For the regime in which surface-wave-induced velocities dominate the velocity field, $t^* < 12.78$, there is evidence of an inertial sub-range. The width of the sub-range decreases as the surface waves propagate away, and the coherent vortex becomes apparent within the ensemble-averaged flow. In figure 12(d–f) we see a region in which the spectrum decreases less rapidly than $k^{-5/3}$ before beginning to roll off at $k_1 = 350$–400 rad m^{-1}. These spectral 'bumps' have been reported previously in the literature for both field measurements (Doron *et al.* 2001; Nimmo Smith, Katz & Osborn 2005) and high-Reynolds-number flows in the laboratory (Saddoughi & Veeravalli 1994). They have been attributed to a 'bottleneck' phenomenon in which the spectral flux of energy from low wavenumbers exceeds the rate of dissipation at the small scales, causing a build-up of energy near the boundary between an inertial sub-range and the dissipation range.

The wavenumber spectra at $x^* = 0.54$ and $x^* = 0.84$ are shown in figure 12(g–l) for $E_{11}(k_3)$ and $E_{33}(k_3)$. At $t^* = 3.42$ the core of the turbulent cloud is at $x^* \approx 0.54$. For $t^* = 3.42 - 12.78$ there is a marked difference at the low wavenumbers due to strong vertical flows in the k_3-direction caused by the surface waves. We also see evidence of an inertial sub-range for $t^* = 3.42$ and 12.78. The turbulent cloud is propagating to the right, and as the flow evolves we expect the turbulent velocity at the downstream location to be larger in magnitude for a given value of $t^* > 3.42$, as the cloud is advected towards $x^* = 0.84$, consistent with what is seen in figure 12(i–l). After the surface waves have passed, the difference in energy density near 12 rad m^{-1} diminishes, and between 200–300 rad m^{-1} the spectra at both locations begin to flatten out. As for the spectra in the k_1-direction, this may be caused by a build-up of energy within these scales, as energy is transported down the spectrum at the larger scales faster than it is dissipated at the smaller scales.

This is shown more clearly in figure 13, which shows $E_{11}(k_1)$ for various values of t^* and z^*. A large inertial sub-range is present near the surface, which decreases for later times and shows evidence of energy accumulating at larger wavenumbers. For k within the inertial sub-range, an estimate of the dissipation rate can be found by

$$E_{11}(k_1) = C_1 \epsilon^{2/3} k_1^{-5/3}, \tag{5.2}$$

where ϵ is the dissipation rate per unit mass and C_1 is a constant shown experimentally to be ≈ 0.5 (Sreenivasan 1995). We see that the magnitude of E_{11} decreases with depth; so if (5.2) holds, then this would suggest that the dissipation rate should decrease as well. If the flux of energy at a given time were approximately constant across the depth of the turbulent region, then there could be a greater tendency towards accumulation of energy with depth.

We can extend the spectra to higher wavenumbers by using wavenumber spectra computed from the mosaic DPIV, which extends the Nyquist wavenumber from $k = 781$ rad m^{-1} out to $k = 2026$ rad m^{-1}. The magnitudes of the spectra computed from the mosaic DPIV vary due to the inhomogeneity of the turbulent cloud, but overall they have the same spectral shape. The mosaic DPIV spectra shown in figure 14 do not exhibit the roll-off seen in the full-field spectra at $k \approx 400$ rad m^{-1} (in figure 14c–h). This would suggest that the approximate $-5/3$ slope seen in figure 12(c–f) is not an extension of the inertial sub-range at high wavenumbers. In other words energy is not being stored at wavenumbers within a larger apparent inertial sub-range.

6. Turbulent kinetic energy budget

The distribution of TKE is governed by (2.3). The pressure field cannot be measured, and thus we cannot describe the pressure-work term. For large Reynolds numbers
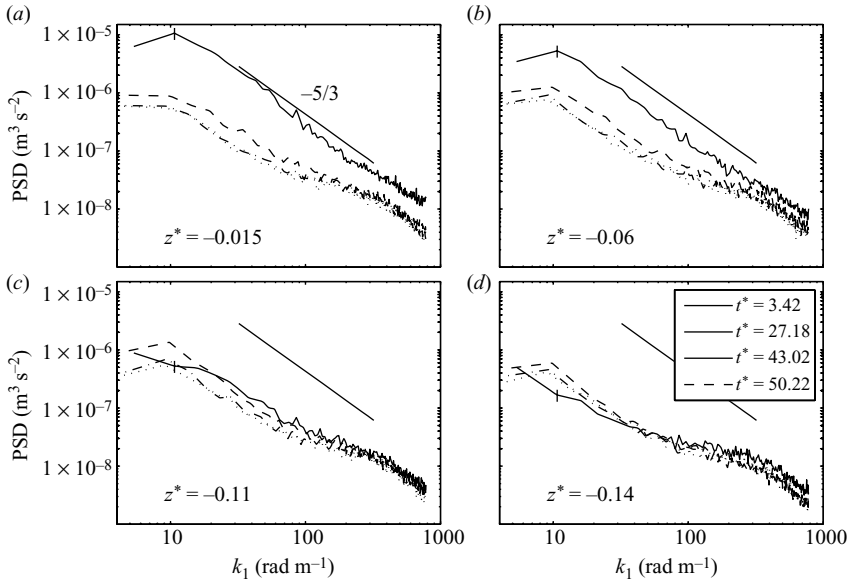
FIGURE 13. Spectra of u in the x_1-direction, $E_{11}(k_1)$, for $t^* = [3.42, 27.18, 43.02, 58.86]$ at (a) $z^* = -0.015$, (b) $z^* = -0.06$, (c) $z^* = -0.11$ and (d) $z^* = -0.14$. The solid black line has a slope of $-5/3$, and its level is kept fixed for all four figures. Confidence levels of 95 % are shown at $k_1 = 10$ rad m^{-1} for spectra at all depths.

the viscous transport term becomes smaller than the other transport terms and will be neglected.

The dissipation term, ϵ, acts on scales near the Kolmogorov length scale defined as

$$\eta_k = \left(\frac{v^3}{\epsilon}\right)^{1/4}. \tag{6.1}$$

Estimates of ϵ from the wavenumber spectra put the smallest Kolmogorov length scale at $\eta_k \approx 0.4$ mm, which is an order of magnitude smaller than the spatial resolution of our velocity estimates. Thus we cannot measure ϵ directly at this resolution; however, we can measure it indirectly. Earlier analysis in §4 focused on estimating dissipation based on homogeneous, isotropic flows with r.m.s. velocities and Taylor microscales similar to those in our case. The tenuous existence of an inertial sub-range and the fact that our flow is not isotropic or homogeneous emphasizes the necessity of finding alternate methods of computing the dissipation rate.

Consider a volume that entirely encompasses the turbulent cloud on the boundaries of which u_i goes to zero (U_i is non-zero on the boundary due to the surface-wave-induced velocity; see figure 2). If we take the integral of (2.3) over this volume we obtain

$$\int_V \frac{\partial q}{\partial t} \, \mathrm{d}V + \int_S (qU_j) \cdot \mathbf{n} \, \mathrm{d}S = -\int_V \langle u_i u_j \rangle \, S_{ij} \, \mathrm{d}V - \int_V \epsilon \, \mathrm{d}V, \tag{6.2}$$

where $q = 1/2 \langle u_i u_i \rangle$. The turbulent-transport term can also be written in terms of a surface integral, but it vanishes, since $u_i = 0$ on the edges of the control volume. We can then infer the volume-integrated dissipation rate from the balance of the integrated evolution, production and advection terms.
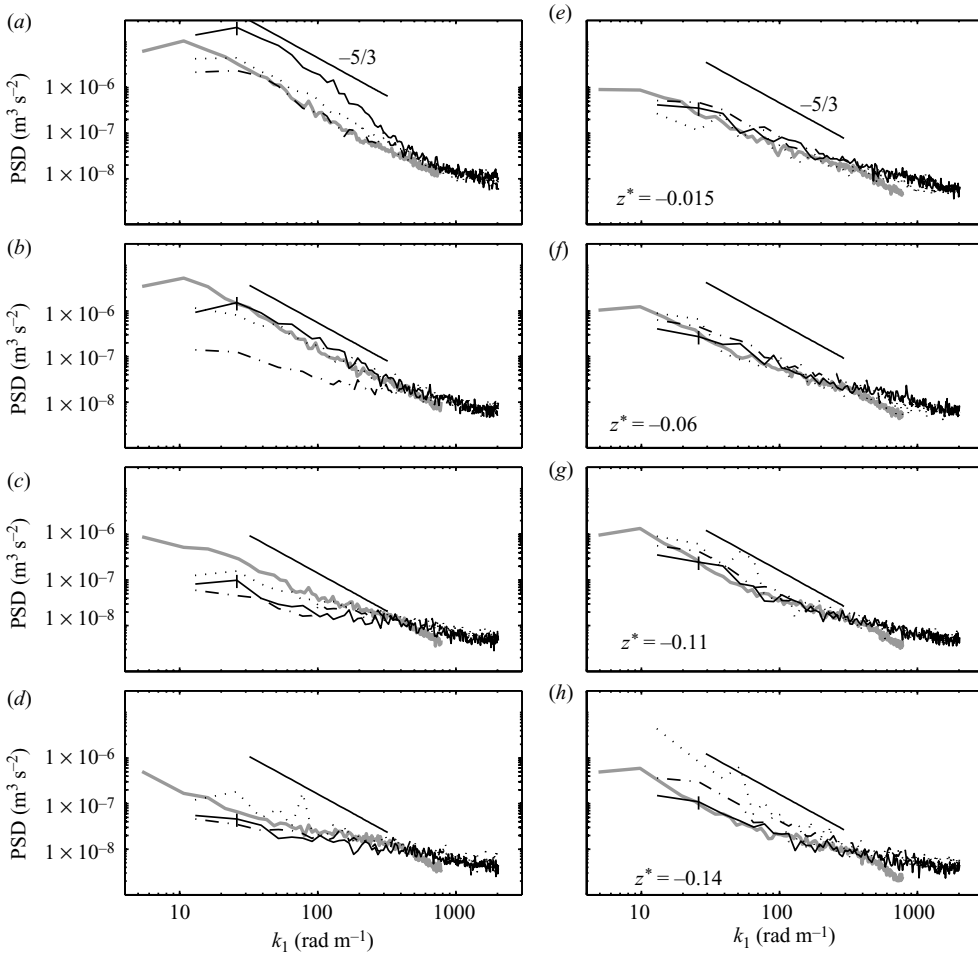
FIGURE 14. Comparison of $E_{11}(k_1)$ for both the full-field measurements and mosaic DPIV at (a–d) $t^* = 3.42$ and (e–h) $t^* = 27.18$; E_{11} from window 1 (⋯), window 2 (——) and window 3 (— ⋅ —). The full-field spectra are shown as grey lines. The panels correspond to four vertical locations, (a, e) $z^* = -0.019$, (b, f) $z^* = -0.06$, (c, g) $z^* = -0.11$ and (d, g) $z^* = -0.15$. The solid black lines have a slope of $k^{-5/3}$, and 95 % confidence limits are shown at $k_1 = 30$ rad m^{-1}.

We can evaluate (6.2) in this plane after making some assumptions about the transverse velocity $\tilde{v}$. We assume that the flow is two-dimensional in the mean, so $\langle \tilde{v} \rangle \approx 0$ and $\partial \langle \rangle / \partial y$ terms vanish. The four locations at which we have (u, v, w) occur within the extent of the turbulent cloud, so through comparison of the spatially and temporally averaged values of q in both two and three dimensions at locations 1–4 we find that

$$q = \frac{1.53}{2}(\langle u^2 \rangle + \langle w^2 \rangle), \qquad (6.3)$$

where q is the full three-dimensional TKE density (see Appendix for further details).

The DPIV measurement region is considered to be two-dimensional in the mean, so the volume and surface integrals become area and line integrals, multiplied by a constant width. The horizontal extent of the integration is shown by the vertical
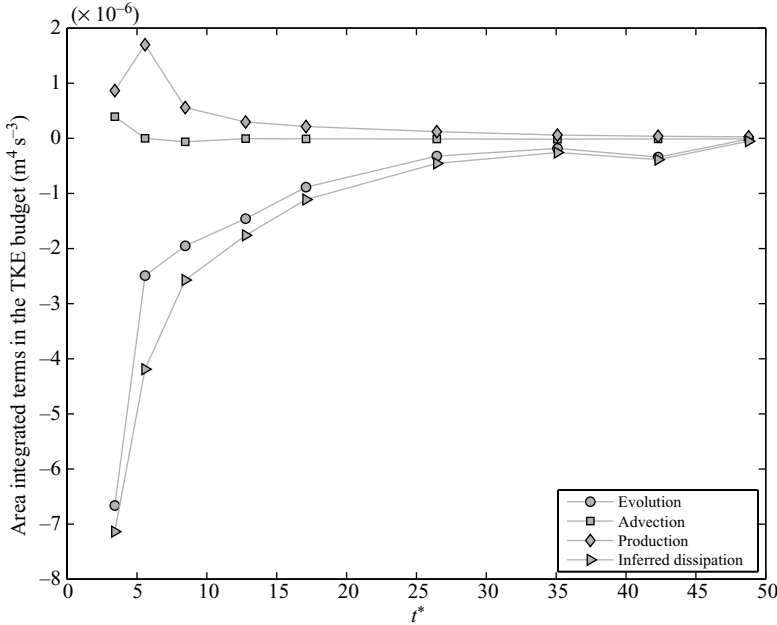
FIGURE 15. Area-integrated values of selected terms in the TKE budget (m^4 s^{-3}). Terms shown are evolution, advection, production, and the inferred dissipation (6.2).

white lines in figure 5, and the vertical extent is from $z^* = -0.23$ to $z^* = 0.05$ (in order to completely encompass the free surface at times near breaking). The inferred dissipation for $t^* = 3.42 - 58.86$ is shown in figure 15 and is seen to be larger in magnitude than both the production and evolution terms. The production term increases slightly between $t^* = 3.42$ and $t^* = 5.58$, consistent with the emergence of the coherent vortex when the surface-wave-induced velocities have been removed (see also Drazen 2006). For later times it suggests that there is little exchange of energy between the coherent structure in the mean flow and the turbulent field (which appears to simply advect the turbulence downstream) and that the main mechanism of transfer of TKE occurs through the surface-wave-induced velocities.

6.1. *Dissipation measurements*

We will now compare the estimate of the integrated dissipation rate given in (6.2) with two other methods. The energy-containing eddies of the flow have a representative velocity u_0 and length scale l_0. To within an order of magnitude, the inertial estimate of the dissipation rate ϵ_I is

$$\epsilon_I \approx \frac{u_0^3}{l_0}. \tag{6.4}$$

The outer velocity scaling will be defined as $u_0 \equiv q^{1/2}$, where q is the horizontally averaged TKE density at a given time and depth as defined in (6.3). The horizontal extent of the averaging here is defined by the width of the cloud and therefore decreases with depth. The length scale l_0 is given by the integral length scale (see (4.1)). The expression (6.4) becomes

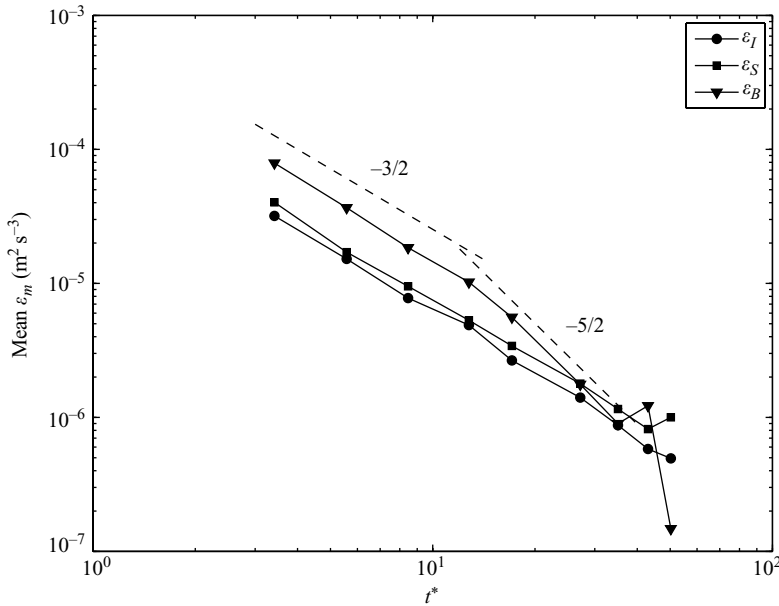$$\epsilon_I = \chi \frac{q^{\frac{3}{2}}}{L_{11}}, \tag{6.5}$$

FIGURE 16. Three estimates of the average dissipation rate per unit mass, ϵ_m. The methods used to compute the estimates are ϵ_I, the inertial estimate of the dissipation rate; ϵ_S, a $k^{-5/3}$ fit to the inertial sub-range of the wavenumber spectra; and ϵ_B, an estimate inferred from the integrated TKE budget (see (6.2)). The dashed lines have a slope of $t^{-3/2}$ and $t^{-5/2}$ as labelled.

where χ is a coefficient determined to be 0.46 in DML and ϵ_I denotes the dissipation rate using the inertial estimate.

We can obtain an estimate of the dissipation rate by fitting a $-5/3$ line within the inertial sub-range of the wavenumber spectra and evaluating (5.2). This will be denoted by ϵ_S. This estimate requires the existence of an inertial sub-range, the length of which was found in § 5 to decrease with both time and depth. If an inertial sub-range is found, this method (along with ϵ_I) has the advantage of being computed over scales which are well resolved by our measurements. These estimates are then vertically averaged from the top to the bottom of the cloud. The inferred dissipation from the integrated production and evolution terms will be denoted by ϵ_B (see (6.2)). The area-averaged dissipation rates are shown in figure 16.

For $t^* < 12.78$, ϵ_I, ϵ_S and ϵ_B all have an apparent $t^{-3/2}$ dependence. After $t^* > 12.78$, ϵ_B follows a $t^{-5/2}$ dependence, while ϵ_S and ϵ_I decay with a dependence closer to $t^{-3/2}$. This similarity between ϵ_I and ϵ_S is not unexpected, since both are based on the assumption that energy is transferred from the large energy-containing scales of the flow to the small dissipative scales of the flow, across an inertial sub-range.

The total dissipation rate of TKE per unit width is given by

$$A\epsilon = \frac{\partial}{\partial t} E_t, \qquad (6.6)$$

where A is the area over which TKE is dissipated and E_t is the total TKE density. The area of the breaking region has been found to grow as $t^{1/2}$, consistent with the findings of RM. We have computed E_t at discrete locations which move with the cloud. The time dependence has been found to be t^{-1}, implying a t^{-2} dependence for $\partial E_t/\partial t$. Thus we expect a $t^{-5/2}$ dependence for ϵ. We see this dependence holds for

$t^* > 12.78$ in figure 16. We have also shown that other terms in the TKE budget are significant for $t^* < 12.78$ (see figure 15), so a deviation from the predicted dependence for these earlier times is not unexpected.

Using acoustic Doppler techniques, Veron & Melville (1999) found a t^{-n} dependence of the dissipation rate, with $n = 1-1.25$. These estimates however are at a single depth and cannot be assumed to have the same dependence as our measure of ϵ, especially due to the inhomogeneous nature of the turbulent cloud. Gemmrich & Farmer (2004) found a $t^{-4.3}$ dependence for ϵ. It should be noted that we and Veron & Melville (1999) have considered single, laboratory breaking events, while Gemmrich & Farmer (2004) measured ϵ from breaking waves in the field, and other processes could contribute to the significant enhancement in the decay of the dissipation rate. RM used measures of the time dependence of the post-breaking area and TKE to find that ϵ should follow a $t^{-5/2}$ dependence, consistent with our findings.

6.2. *Balances in the turbulent kinetic energy budget*

As stated previously, the measurements in the longitudinal plane encompass the entire turbulent cloud and will be used to compute horizontally integrated terms in the TKE budget, with the integration over the horizontal extent of the turbulent cloud. Despite the large ensemble in the longitudinal plane, at later times the signals are still quite noisy with the turbulent-transport term exhibiting the most noise. This is due to the lower signal to noise ratio from the DPIV measurements as the magnitude of the flow velocity decreases at large t^*. In order to separate the noise from the signal we first compute the vertical wavenumber spectrum of the horizontally integrated turbulent-transport term from $z^* = -0.44$ to $z^* = -0.25$, where the signal is entirely noise, as it is in a region outside of the turbulent cloud.

A separation between the low-wavenumber end of the spectrum and the high-wavenumber regime is seen to occur at $k_3 = 130 \, \text{rad m}^{-1}$ (see Drazen 2006 for further details). We then low-pass filter the horizontally integrated terms in the TKE budget, using a running-mean filter with a width corresponding to $k_3 = 130 \, \text{rad m}^{-1}$.

The presence of surface waves within the measurement region complicates the computation of these terms, as the location of the turbulent cloud changes with the free surface as the waves pass. To simplify comparisons between terms the horizontal integrals are cut off at a depth corresponding to the lowest point in the free surface at a given value of t^*.

The horizontally integrated evolution, advection, production, turbulent transport and dissipation are shown in figure 17 for $t^* = [3.42, 5.58, 8.46, 12.78, 17.10, 27.18]$. The dissipation is computed using the inertial estimate defined in (6.5) and is only shown over the depth of the cloud, as r.m.s. values of u were not computed below this. Also given over the depth of the cloud is the residual obtained when the measured terms are moved to the right-hand side of the TKE budget equation. We can see that at $t^* = 3.42$ the advection term dominates, due to the large vertical velocity associated with the surface waves. By $t^* = 5.58$ the advection term has changed sign, but the remaining terms in the budget are now of the same approximate magnitude. For the terms shown, there is an approximate balance between the evolution and advection terms and also between the production, dissipation and turbulent-transport terms. There is a predominately negative transport near the surface, which becomes positive at depth. We see similar results for $t^* = 8.46$ but with the advection term changing sign near the surface while remaining positive at depth. The dissipation term has also increased in magnitude and is the dominant term (along with the evolution) for the remainder of the times considered. The approximately constant value of the evolution term below $z^* = -0.2$ is attributed to the presence of a long wave in the
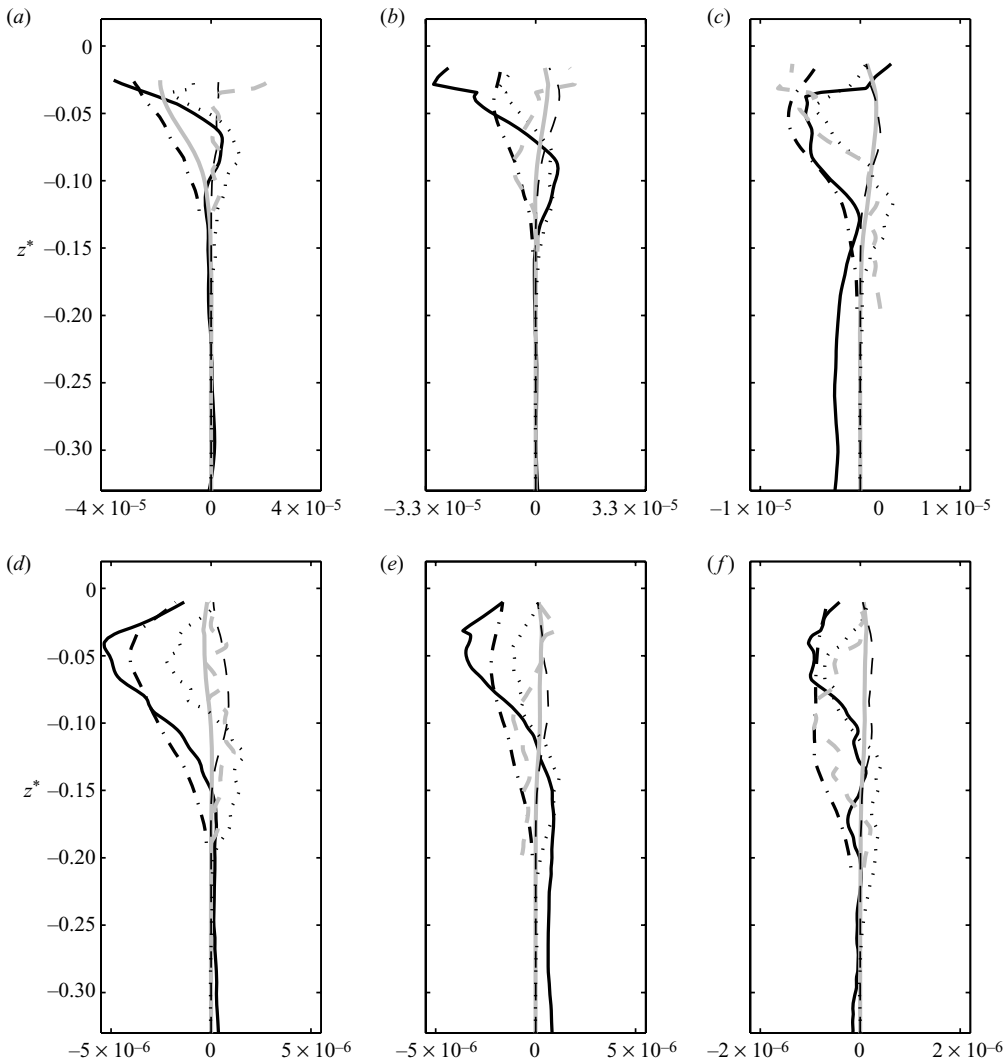
FIGURE 17. Horizontal integrals of non-dimensional terms in the TKE budget in the longitudinal plane for (a) $t^* = 3.42$, (b) $t^* = 5.58$, (c) $t^* = 8.46$, (d) $t^* = 12.78$, (e) $t^* = 17.10$ and (f) $t^* = 27.18$. The flow was assumed to be two-dimensional in the mean (i.e. terms $\partial\langle\rangle/\partial y = 0$). The terms shown are evolution (—), advection (—), production (——), turbulent transport ($\cdots$), dissipation using (6.5) ($-\cdot-$) and residual (——). Note the change in horizontal scale between each sub-figure.

tank generated by the breaking process; a similar result is seen at $t^* = 17.10$ and is consistent with a long wave propagating upstream and reflecting off the paddle.

For $t^* > 12.78$ we see similar profiles, with the advection term decreasing significantly as the surface waves leave the measurement region. The production term also decreases leaving the evolution, transport and dissipation terms as the remaining dominant terms. As noted earlier, this change in the production term suggests that after breaking the main exchange of energy with the turbulence is through the surface waves and that the only further interaction between the mean and turbulent fields is the slow advection downstream of the turbulence by the coherent vortex.

These measurements contrast with Chang & Liu (1999; CL) who studied quasi-periodic breaking using DPIV in the longitudinal plane along the centreline of a wave tank. In order to account for v, a scaling factor derived from shear flows was used (Svendsen 1987),

$$q = \frac{1.33}{2}(\langle u^2 \rangle + \langle w^2 \rangle). \tag{6.7}$$

CL found an apparent balance between advection, production and dissipation within a few wave periods. Their estimate of the dissipation rate was computed from a balance of the remaining terms within the measurement region. The quasi-steady breaking described by CL appears to be forced by the wavemaker, as the breaking occurs less than a wavelength from the wavemaker, $\lambda = 1.21$ m, $x_b = 0.38$ m. This apparent forcing (combined with the shallower depth of the water), the important role of the bottom boundary condition and the quasi-periodic nature of their breaking yield results which cannot be directly compared with our unsteady deep-water breaking.

In their stochastic model of breaking, Sullivan *et al.* (2004) presented terms in the TKE budget for Couette flow and shear-driven flow as well as flow driven entirely by breaking. The estimates of the energy budget terms show a distinct difference from those obtained by CL. Consistent with our findings, the turbulent-transport term is significant near the surface. Additionally they found that the pressure-transport term is of the same order of magnitude as production. If the residual term given in our figure 17 is representative of the pressure-work term, then we also see an approximate balance between production and the pressure-transport term. While some of these similarities support our findings it is important to note that the flow is qualitatively different from what we measured in the laboratory. This is because their results are based on multiple three-dimensional breaking events across their computational domain, while we have a single two-dimensional (in the mean) breaking event. Further numerical modelling may help to elucidate the role of pressure transport which is currently not measurable using techniques described in this paper.

As an appendix to their paper on laboratory measurements, MVW presented tentative estimates of the terms in the TKE budget; tentative because of the relatively small ensemble used and the velocity field reconstruction using a collage of windows. As for CL, MVW used an approximation for v to account for the unmeasured out-of-plane velocity, using

$$q = \frac{1.5}{2}\langle u^2 + w^2 \rangle \tag{6.8}$$

which assumes that $v^2 = (u^2 + w^2)/2$. To account for the dissipation rate the isotropic estimate (4.5) was used, and the terms were then averaged horizontally. They presented results between three and five wave periods after breaking with the shape and relative magnitude of the horizontally integrated terms comparing well to our findings considering the differences in the experiments. They found a relative balance between the advection and transport terms between these times after breaking. These balances however must be interpreted carefully as the surface-wave-induced velocity has been shown to change the sign of the advection term (see figure 17(*b*, *c*)).

7. Discussion

7.1. *Wavenumber spectra maxima*

We have measured the turbulent velocity field beneath deep-water breaking waves using a high-resolution DPIV system. The ability to directly image the whole flow

obviates the need to reconstruct the flow field with a large number of windows and permits computation of the wavenumber spectra as described in §5.

The wavenumber spectra presented exhibit a feature in which the spectrum falls off slower than $k^{-5/3}$ for wavenumbers higher than the apparent inertial sub-range in the k_1- and k_3-directions. These local maxima have also been seen previously in both the field and the laboratory, using a variety of measurement techniques. The feature persists when we extend the cutoff wavenumber from $\approx 700\,\mathrm{rad\,m^{-1}}$ to $\approx 2000\,\mathrm{rad\,m^{-1}}$ and is larger than can be explained by any residual wave motion in the tank at those wavenumbers.

The range of Taylor microscale Reynolds numbers encountered here suggests that the inertial sub-range, if it were to exist, should have a a bandwidth which is larger by an order of magnitude than that seen for $t^* > 3.42$ (Pope 2000). Due to the freely decaying nature of the turbulence the Reynolds number may not be sufficiently large to allow the traditional $k^{-5/3}$ dependence within the inertial sub-range. The existence of these local maxima, which yield limited inertial sub-ranges and the anisotropy, underscore issues in estimating dissipation rates from the measured wavenumber spectra. Alternate methods such as those used in §6.1 may be more appropriate.

The source of the maxima is thought to be due to a build-up of energy in scales near the boundary between a weak inertial sub-range and the dissipation range. The cause of this build-up is thought to be from an inability of the flow to dissipate energy faster than the rate at which energy is transported down from the larger scales.

8. Conclusions

We have presented measurements of the large-scale turbulent structure of breaking waves in the laboratory using DPIV. We have provided a description of the breaking process and the subsequent dynamics which will support numerical modelling efforts such as those of Sullivan *et al.* (2004, 2007). Any insight into the complex nature of these types of flow can serve as a valuable tool in guiding the modelling of the post-breaking wave field.

The large coherent vortex seen by RM and MVW is seen here with a sufficient spatial scale to image the whole vortex at once. The initial formation of the breaking region is rapid, occurring within three wave periods after breaking. The depth of the ensemble-averaged mixed region is seen to follow a $x^{1/2}$ dependence and permits the measurement of an eddy viscosity, ν_T.

The wavenumber spectra exhibit an inertial sub-range near the surface for small t^*. A region in which the spectra become less steep than $k^{-5/3}$ leads to the formation of a local maximum. The formation of this local maximum appears to be consistent with an imbalance between the energy flux from the large scales and the viscous dissipation at small scales.

The experimental configuration allows us to measure all three components of (u, v, w) at four vertical locations within the flow. Comparison of the TKE using both (u, w) and (u, v, w) has shown that $q = 1.53q'$, where q' is the TKE in the longitudinal plane and q is the full three-dimensional TKE.

While the local dissipation rate $\epsilon = 2\nu s_{ij}s_{ij}$ could not be directly measured, we can infer a value from an implied balance of terms in the volume-integrated TKE budget. Comparisons of the inferred dissipation ϵ_B with integral measures of the dissipation rate using inertial and spectral estimates show good agreement with the inertial and spectral estimates having the benefit of being computed over scales easily resolved with the current experimental set-up.

The area-integrated TKE density is seen to follow an approximate $t^{-0.75}$ dependence while the surface waves are present and then begins to decay faster for $t^* > 12.78$. The advection term is significant for $t^* \leqslant 17.10$ and is the dominant term at $t^* = 3.42$, due to the surface-wave-induced velocities. The turbulent-transport and evolution terms are seen to be significant for $t^* \geqslant 5.58$. Production is significant for $5.58 < t^* < 17.10$ and decreases in magnitude with time but is still non-zero for later times. The small magnitude of production for larger t^* implies that the main exchange of energy from the mean field to the turbulence occurs via the velocities induced by the surface waves. At later times the coherent vortex advects the turbulent cloud downstream.

The breaking parameter discussed at length in DML was estimated from the distribution of momentum flux using the Reynolds stress in figure 6 using the methodology of MVW. For the experimental conditions used here, $b = 0.015$, while b measured by DML was $b = 0.022$. The inertial scaling of wave dissipation due to breaking developed by DML predicts $b = 0.021$ (see figure 13 in that work). Small errors in estimating the speed of the advancing front can become significant when estimating b and could account for some of the variability found.

Appendix. Comparison of turbulent kinetic energy density in two and three dimensions

The DPIV technique used here gives only two components of the flow velocity vector. The mean flow can be considered two-dimensional, but the turbulence is inherently three-dimensional, and the missing component needs to be accounted for in the absence of out-of-plane measurements.

Svendsen (1987) presented measurements of TKE under surf-zone waves and argued that they exhibited characteristics of plane wakes based on the results of Battjes & Sakai (1981) from quasi-steady breaking. To account for the transverse v component, the relative strengths of (u^2, v^2, w^2) for a plane wake were used and the TKE density, q, was assumed to be

$$q = \frac{1.33}{2}(\langle u^2 \rangle + \langle w^2 \rangle). \tag{A 1}$$

CL used this estimate of q to account for the missing component v in DPIV measurements of quasi-periodic breaking in the laboratory. RM presented LDA measurements of unsteady breaking in the laboratory and used $\langle v^2 \rangle = \langle w^2 \rangle$, since $\langle u^2 \rangle > \langle w^2 \rangle$.

Previously MVW made the assumption

$$\langle v^2 \rangle \approx \frac{1}{2}(\langle u^2 \rangle + \langle w^2 \rangle) \tag{A 2}$$

which yields

$$q = \frac{1.5}{2}(\langle u^2 \rangle + \langle w^2 \rangle). \tag{A 3}$$
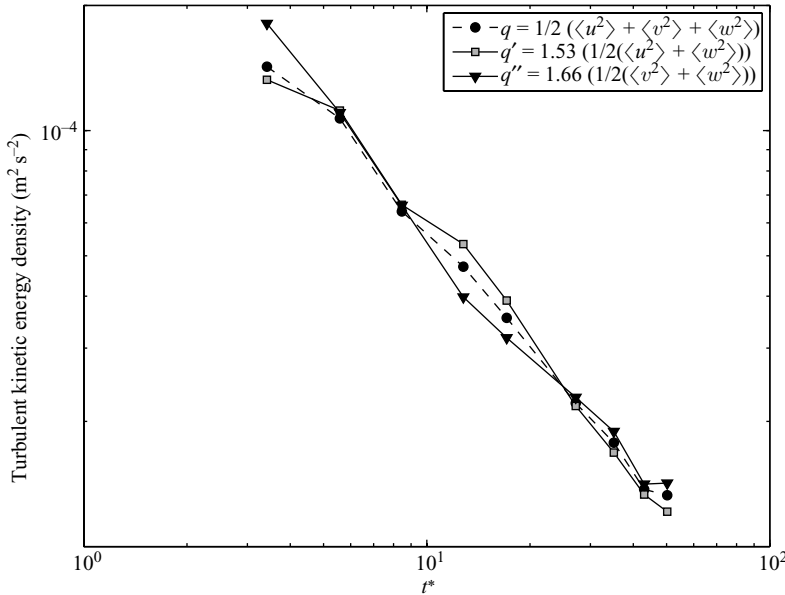
FIGURE 18. Comparison between the area-averaged two-dimensional estimate of TKE density in the longitudinal plane $q' = 1.53(1/2(\langle v^2 \rangle + \langle w^2 \rangle))$ and the transverse plane $q'' = 1.66(1/2(\langle v^2 \rangle + \langle w^2 \rangle))$ as well as the area-averaged three-dimensional measurement of q.

The present measurements allow comparison of the estimate of q from the longitudinal plane with the full three-dimensional field at the four cross-stream locations. To estimate the necessary scaling factor in each plane we first average vertically and then horizontally,

$$\overline{q}, \overline{q'}, \overline{q''} = \frac{1}{Z(x_2^* - x_1^*)} \int_{x_1^*}^{x_2^*} \int_{-H}^{\eta} q, q', q'' \, dz^* \, dx^*, \tag{A 4}$$

where $Z = \eta + H$; x_1, x_2 are the horizontal limits of integration; and the overbar denotes an area average. The two-dimensional TKE density in the longitudinal plane is given by $q' = 1/2\langle u^2 + w^2 \rangle$ and by $q'' = 1/2\langle v^2 + w^2 \rangle$ in the transverse plane. The three-dimensional TKE density, q, is estimated by

$$q = \frac{1}{2} \left(\left\langle u^2 + \frac{w|_L^2}{2} \right\rangle + \left\langle v^2 + \frac{w|_T^2}{2} \right\rangle \right), \tag{A 5}$$

where $w|_L$ and $w|_T$ are measurements of w in the longitudinal and transverse planes respectively.

The relative magnitude of u, v and w can be seen to change with time, so we take the temporal average to define a mean scaling factor,

$$\frac{1}{t_2 - t_1} \int_{t_1}^{t_2} \frac{\overline{q}}{\overline{q'}} \, dt = 1.53, \tag{A 6}$$

$$\frac{1}{t_2 - t_1} \int_{t_1}^{t_2} \frac{\overline{q}}{\overline{q''}} \, dt = 1.66. \tag{A 7}$$

A comparison between the mean value of $\overline{q(t)}$, $1.53\,\overline{q'(t)}$ and $1.66\,\overline{q''}$ is shown in figure 18.

REFERENCES

BANNER, M. L. & PEREGRINE, D. H. 1993 Wave breaking in deep water. *Annu. Rev. Fluid Mech.* **25**, 373–397.

BATTJES, J. A. & SAKAI, T. 1981 Velocity field in a steady breaker. *J. Fluid Mech.* **111**, 421–437.

BONMARIN, P. J. 1989 Geometric properties of deep-water breaking waves. *J. Fluid Mech.* **209**, 405–433.

CHANG, K.-A. & LIU, P. L.-F. 1998 Velocity, acceleration, and vorticity under a breaking wave. *Phys. Fluids* **10**, 327–329.

CHANG, K.-A. & LIU, P. L.-F. 1999 Experimental investigation of turbulence generated by breaking waves in water of intermediate depth. *Phys. Fluids* **11**, 3390–3400.

CHANG, K.-A. & LIU, P. L.-F. 2000 Psuedo turbulence in PIV breaking-wave measurements. *Exp. Fluids* **29**, 331–338.

CHEN, G., KHARIF, C., ZALESKI, S. & LI, J. 1999 Two-dimensional Navier–Stokes simulation of breaking waves. *Phys. Fluids* **11**, 121–133.

DORON, P., BERTUCCIOLI, L., KATZ, J. & OSBORN, T. R. 2001 Turbulence characteristics and dissipation estimates in the coastal ocean bottom boundary layer from PIV data. *J. Phys. Oceanogr.* **31**, 2108–2131.

DRAZEN, D. A. 2006 Laboratory studies of nonlinear and breaking surface waves. PhD thesis, University of California, San Diego.

DRAZEN, D. A., MELVILLE, W. K. & LENAIN, L. 2008 Inertial estimates of dissipation in unsteady breaking waves. *J. Fluid Mech.* **611**, 307–332.

DUNCAN, J. H. 1981 An experimental investigation of breaking waves produced by a towed hydrofoil. *Proc. R. Soc. Lond.* A **377**, 331–348.

DUNCAN, J. H. 1983 The breaking and non-breaking wave resistance of a two-dimensional hydrofoil. *J. Fluid Mech.* **126**, 507–520.

DUNCAN, J. H. 2001 Spilling breakers. *Annu. Rev. Fluid Mech.* **33**, 519–547.

GEMMRICH, J. R. & FARMER, D. M. 2004 Near-surface turbulence in the presence of breaking waves. *J. Phys. Oceanogr.* **34**, 1067–1086.

GONZALEZ, R. C. & WOODS, R. E. 2002 *Digital Image Processing*, 2nd ed. Prentice Hall.

LAMARRE, E. 1993 An experimental study of air entrainment by breaking waves. PhD thesis, MIT–Woods Hole Oceanographic Institution.

LAMARRE, E. & MELVILLE, W. K. 1991 Air entrainment and dissipation in breaking waves. *Nature* **351**, 469–472.

LIN, J. C. & ROCKWELL, D. 1995 Evolution of a quasi-steady breaking wave. *J. Fluid Mech.* **302**, 29–44.

LOEWEN, M. R. 1991 Laboratory measurements of the sound generated by breaking waves. PhD thesis, MIT–Woods Hole Oceanographic Institution.

LOEWEN, M. R. & MELVILLE, W. K. 1991 Microwave backscatter and acoustic radiation from breaking waves. *J. Fluid Mech.* **224**, 601–623.

LONGUET-HIGGINS, M. S. 1974 Breaking waves – in deep or shallow water. In *Proceedings of the 10th Symposium on Naval Hydrodynamics* (ed. R. D. Cooper & S. D. Doroff), pp. 597–605. Office of Naval Research.

MELVILLE, W. K. 1996 The role of surface-wave breaking in air–sea interaction. *Annu. Rev. Fluid Mech.* **28**, 279–321.

MELVILLE, W. K., VERON, F. & WHITE, C. 2002 The velocity field under breaking waves: coherent structures and turbulence. *J. Fluid Mech.* **454**, 203–233.

NIMMO SMITH, W. A. M., KATZ, J. & OSBORN, T. 2005 On the structure of turbulence in the bottom boundary layer of the coastal ocean. *J. Phys. Oceanogr.* **35**, 72–93.

PERLIN, M., HE, J. & BERNAL, L. P. 1996 An experimental study of deep water plunging breakers. *Phys. Fluids* **8** (9), 2365–2374.

PHILLIPS, O. M. 1985 Spectral and statistical properties of the equilibrium range in wind-generated gravity waves. *J. Fluid Mech.* **156**, 505–531.

POPE, S. B. 2000 *Turbulent Flows*. Cambridge University Press.

RAFFEL, M., WILLERT, C. & KOMPENHANS, J. 1998 *Particle Image Velocimetry*. Springer.

RAPP, R. J. & MELVILLE, W. K. 1990 Laboratory measurements of deep-water breaking waves. *Phil. Trans. R. Soc. Lond.* A **331**, 735–800.

SADDOUGHI, S. G. & VEERAVALLI, S. V. 1994 Local isotropy in turbulent boundary layers at high Reynolds number. *J. Fluid Mech.* **268**, 333–372.

SREENIVASAN, K. R. 1995 On the universality of the Kolmogorov constant. *Phys. Fluids* **7** (11), 2778–2784.

SULLIVAN, P. P., MCWILLIAMS, J. C. & MELVILLE, W. K. 2004 The oceanic boundary layer driven by wave breaking with stochastic variability. Part 1. Direct numerical simulations. *J. Fluid Mech.* **507**, 143–174.

SULLIVAN, P. P., MCWILLIAMS, J. C. & MELVILLE, W. K. 2007 Surface gravity wave effects in the oceanic boundary layer: large-eddy simulation with vortex force and stochastic breakers. *J. Fluid Mech.* **593**, 405–452.

SVENDSEN, I. A. 1987 Analysis of surf zone turbulence. *J. Geophys. Res.* **92** (C5), 5115–5130.

TENNEKES, H. & LUMLEY, J. L. 1972 *A First Course in Turbulence*. MIT Press.

VERON, F. & MELVILLE, W. K. 1999 Pulse-to-pulse coherent doppler measurements of waves and turbulence. *J. Atmos. Ocean. Technol.* **16**, 1580–1597.

WATANABE, Y., SAEKI, H. & HOSKING, R. J. 2005 Three-dimensional vortex structures under breaking waves. *J. Fluid Mech.* **545**, 291–328.

WILLERT, C. E. 1997 Stereoscopic digital particle image velocimetry for application in wind tunnel flows. *Meas. Sci. Technol.* **8**, 1465–1479.